J|A|C|S
ARTICLES
Published on Web 10/10/2007

Electronic Structure of the Mn_4O_xCa Cluster in the S_0 and S_2 States of the Oxygen-Evolving Complex of Photosystem II Based on Pulse ^{55}Mn-ENDOR and EPR Spectroscopy

Leonid V. Kulik,*,† Boris Epel, Wolfgang Lubitz,* and Johannes Messinger*

Contribution from the Max Planck Institute for Bioinorganic Chemistry, Stiftstrasse 34-36, D-45470 Mülheim an der Ruhr, Germany

Received March 2, 2007; E-mail: chemphy@ns.kinetic.nsc.ru; lubitz@mpi-muelheim.mpg.de; messinger@mpi-muelheim.mpg.de

Abstract: The heart of the oxygen-evolving complex (OEC) of photosystem II is a Mn_4O_xCa cluster that cycles through five different oxidation states (S_0 to S_4) during the light-driven water-splitting reaction cycle. In this study we interpret the recently obtained ^{55}Mn hyperfine coupling constants of the S_0 and S_2 states of the OEC [Kulik et al. *J. Am. Chem. Soc.* **2005**, *127*, 2392−2393] on the basis of Y-shaped spin-coupling schemes with up to four nonzero exchange coupling constants, *J*. This analysis rules out the presence of one or more Mn(II) ions in S_0 in methanol (3%) containing samples and thereby establishes that the oxidation states of the manganese ions in S_0 and S_2 are, at 4 K, Mn_4(III, III, III, IV) and Mn_4(III, IV, IV, IV), respectively. By applying a "structure filter" that is based on the recently reported single-crystal EXAFS data on the Mn_4O_xCa cluster [Yano et al. *Science* **2006**, *314*, 821−825] we (i) show that this new structural model is fully consistent with EPR and ^{55}Mn-ENDOR data, (ii) assign the Mn oxidation states to the individual Mn ions, and (iii) propose that the known shortening of one 2.85 Å Mn−Mn distance in S_0 to 2.75 Å in S_1 [Robblee et al. *J. Am. Chem. Soc.* **2002**, *124*, 7459−7471] corresponds to a deprotonation of a μ-hydroxo bridge between Mn_A and Mn_B, i.e., between the outer Mn and its neighboring Mn of the μ_3-oxo bridged moiety of the cluster. We summarize our results in a molecular model for the $S_0 \rightarrow S_1$ and $S_1 \rightarrow S_2$ transitions.

Introduction

Photosystem II (PSII) is the unique enzyme that splits water into molecular oxygen, protons, and "energy rich" electrons utilized for CO_2 fixation. This solar energy driven reaction evolved about 2.5 billion years ago[1] and created the present day oxygen level of ∼21% in our atmosphere. It is expected that unraveling the structural and functional principles of the catalytic site of water oxidation will inspire the development of artificial catalysts for solar light powered water splitting into molecular oxygen and hydrogen. Such a process appears to be best suited for a sustainable generation of H_2 or other energy carriers.[2−11]

In PSII the four-electron oxidation of two water molecules is catalyzed by a functional unit, which is known as the oxygen-evolving complex (OEC) or water-oxidizing complex (WOC). The OEC consists of an inorganic core comprising four manganese, one calcium, and at least five oxygen bridges (Mn_4O_xCa cluster) that is surrounded by a functionally important protein matrix. Cofactors are Cl^- and possibly bicarbonate.[12−14]

During the catalytic cycle (Kok cycle) the OEC passes through five different redox states (S_n states, S_0 to S_4).[15] The advancement of the OEC to the next higher S_n state occurs after the absorption of a suitable light quantum by a chlorophyll molecule of the PSII antenna, which transfers the excitation energy into the reaction center of PSII (P680/Pheo in Figure 1a), where the primary charge separation occurs.[16,17] This

† Permanent address: Institute of Chemical Kinetics and Combustion, Novosibirsk, Russia.

(1) Dismukes, G. C.; Blankenship, R. E. The origin and evolution of photosynthetic oxygen production. In *Photosystem II. The Light-Driven Water:Plastoquinone Oxidoreductase*; Wydrzynski, T., Satoh, K., Eds.; Advances in Photosynthesis and Respiration; Springer: Dordrecht, 2005; Vol. 22, pp 683−695.
(2) Esper, B.; Badura, A.; Rögner, M. *Trends Plant. Sci.* **2006**, *11*, 543−549.
(3) Barber, J. *Biochem. Soc. Trans.* **2006**, *34*, 619−631.
(4) Alstrum-Acevedo, J. H.; Brennaman, M. K.; Meyer, T. J. *Inorg. Chem.* **2005**, *44*, 6802−6827.
(5) Hammarström, L. *Curr. Opin. Chem. Biol.* **2003**, *7*, 666−673.
(6) Sun, L. C.; Hammarström, L.; Akermark, B.; Styring, S. *Chem. Soc. Rev.* **2001**, *30*, 36−49.
(7) Lewis, N. S.; Nocera, D. G. *Proc. Natl. Acad. Sci. U.S.A.* **2006**, *103*, 15729−15735.
(8) Rüttinger, W.; Dismukes, G. C. *Chem. Rev.* **1997**, *97*, 1−24.
(9) Yagi, M.; Kaneko, M. *Chem. Rev.* **2001**, *101*, 21−35.
(10) Rupprecht, J.; Hankamer, B.; Mussgnug, J. H.; Ananyev, G.; Dismukes, C.; Kruse, O. *Appl. Microbiol. Biotechnol.* **2006**, *72*, 442−449.
(11) Kruse, O.; Rupprecht, J.; Mussgnug, J. R.; Dismukes, G. C.; Hankamer, B. *Photochem. Photobiol. Sci.* **2005**, *4*, 957−970.
(12) Hillier, W.; Messinger, J. Mechanism of photosynthetic oxygen production. In *Photosystem II. The Light-Driven Water:Plastoquinone Oxidoredutase*; Wydrzynski, T., Satoh, K., Eds.; Advances in Photosynthesis and Respiration; Springer: Dordrecht, 2005; Vol. 22, pp 567−608.
(13) van Gorkom, H. J.; Yocum, C. F. The calcium and chloride cofactors. In *Photosystem II. The Light-Driven Water:Plastoquinone Oxidoreductase*; Wydrzynski, T., Satoh, K., Eds.; Advances in Photosynthesis and Respiration; Springer: Dordrecht, 2005; Vol. 22, pp 307−328.
(14) van Rensen, J. J. S.; Klimov, V. V. Bicarbonate interactions. In *Photosystem II. The Light-Driven Water:Plastoquinone Oxidoreductase*; Wydrzynski, T., Satoh, K., Eds.; Advances in Photosynthesis and Respiration; Springer: Dordrecht, 2005; Vol. 22, pp 329−346.
(15) Kok, B.; Forbush, B.; McGloin, M. *Photochem. Photobiol.* **1970**, *11*, 457−476.
(16) Renger, G.; Holzwarth, A. R. Primary electron transfer. In *Photosystem II. The Light-Driven Water:Plastoquinone Oxidoreductase*; Wydrzynski, T. J., Satoh, K., Eds.; Advances in Photosynthesis and Respiration; Springer: Dordrecht, 2005; Vol. 22, pp 139−175.
(17) Holzwarth, A. R.; Müller, M. G.; Reus, M.; Nowaczyk, M.; Sander, J.; Rögner, M. *Proc. Natl. Acad. Sci. U.S.A.* **2006**, *103*, 6895−6900.

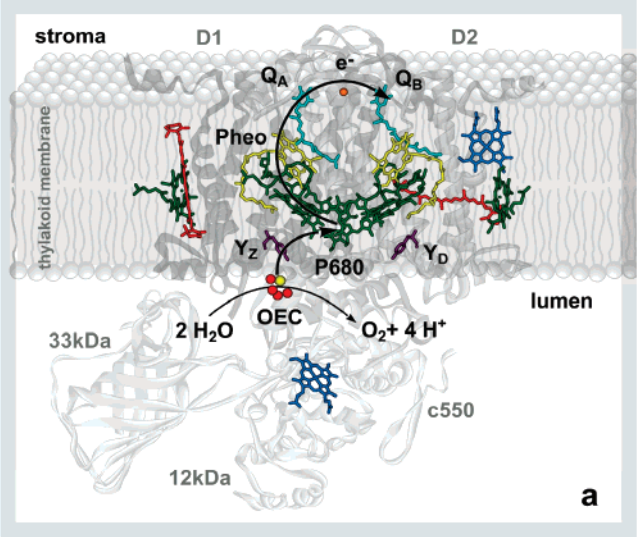

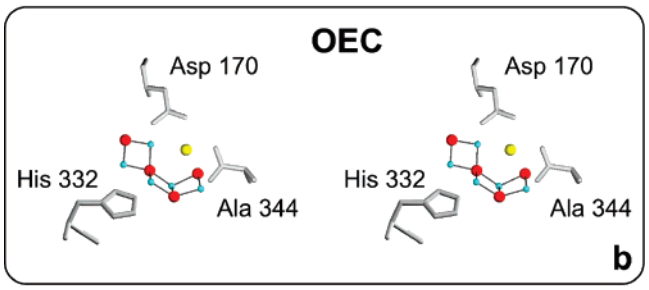

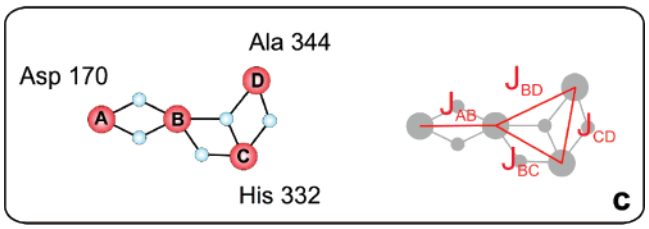

Figure 1. Panel a shows a schematic view of the photosystem II (PSII) complex in the thylakoid membrane that is based on the 3.0 Å crystal structure of Loll et al.[20] For clarity the inner antenna proteins CP43 and CP47, which are involved in harvesting the light energy, and the cytochrome b559 subunits are not shown. The other core proteins of PSII are shown in gray with corresponding labels. The cofactors of the D1, D2, cyt c550, and cyt b559 proteins are placed in color on top of the proteins (see text for more details). Panel b presents a stereoview of the Mn_4O_xCa cluster together with selected ligands that are referred to in this work. The structure shown was derived by Yano et al. on the basis of polarized EXAFS spectroscopy on PSII single crystals (Model III).[21] The view is also approximately along the membrane plane and from a similar angle as that in panel a. Mn ions are shown in red, oxygens, in cyan, and Ca, in yellow. Panel c displays a schematic top view (approximately along the membrane normal) of the Mn_4O_5 core of the Mn_4O_xCa cluster using the same color code as that above. This schematic representation allows a clearer visualization of the bridging motifs between the four Mn ions, which are labeled A, B, C, and D. On the right side of panel c the general coupling scheme is shown that is employed in this study to derive the electronic structure of the S_0 and S_2 states.

triggers a sequence of electron-transfer reactions that result in (i) the one-electron oxidation of the OEC via the redox-active tyrosine Z, Y_Z, of the D1 protein, (ii) an S_n state dependent proton release, and (iii) the reduction of plastoquinone Q_B (via Q_A) on the acceptor side of PSII (Figure 1a). After the accumulation of four oxidizing equivalents (S_4 state) molecular oxygen is formed and released into the medium. In this process also new substrate water binds and the S_0 state is reformed. The current knowledge about photosynthetic water splitting and possible mechanisms for O−O bond formation have recently been discussed in detail.[12,18,19] The intermediate oxidation states of the Kok cycle (S_0 to S_3) can be prepared and trapped in high yields using specific illumination and freezing protocols that start from the dark-stable S_1 state (see Experimental Section).

Knowledge of the structure of the OEC in its different S_n states is highly important for understanding its reactivity. Numerous efforts by different techniques have led recently to a significant improvement in spatial resolution. The basis for most structural suggestions forms a set of 11 different models containing two or three 2.7 Å Mn−Mn distances and one or two 3.3 Å Mn−Mn distances. This set of structures was derived from extended X-ray absorption fine structure (EXAFS) measurements on frozen PSII solutions.[22,23] Additional constraints were obtained from X-ray diffraction (XRD) studies on PSII single crystals, which favor models with an overall Y-shaped arrangement of the Mn ions in the Mn_4O_xCa complex.[20,24−26] In a subsequent XRD study a Mn_3O_4Ca cubane with the fourth Mn attached to this unit via a μ_4-oxo bridge at one of its corners was suggested as the geometric structure of the S_1 state.[27] However, the resolution of all current PSII crystal structures is not high enough to (i) assign precise positions for the four manganese ions and the one calcium ion within the protein matrix and (ii) determine the bridging motifs between these metal ions. Moreover, the current X-ray diffraction data collection conditions lead to a severe impairment of the integrity of the Mn_4O_xCa complex due to radiation damage.[28]

Recently the first reliable geometric structure of the Mn_4O_5 core of the Mn_4O_xCa cluster in the S_1 state was obtained by polarized EXAFS spectroscopy on PSII single crystals.[21] This structure consists of three Mn_2O_2 rhombi (Figure 1b,c). Two of these rhombi have a common Mn−O side (Mn_C−O), while the third rhombus shares one manganese ion (Mn_B) with the μ_3-oxo bridged unit. In this way two 2.7 Å (Mn_A−Mn_B and Mn_B−Mn_C), one 2.8 Å (Mn_C−Mn_D), and one 3.3 Å (Mn_B−Mn_D) distances are created between the four Mn ions. While only this Mn_4O_5 motif was found to reproduce the dichroism of the experimental polarized EXAFS spectra, two possible orientations of this complex in PSII were determined by Yano and co-workers.[21] This resulted in the proposal of four distinct models (I, II, IIa, and III) that also account for (i) correspondingly different positions for Ca^{2+} and (ii) for the relative position of the μ_3-oxo bridge (above or below the Mn_3 plain).[21] Figure

(18) McEvoy, J. P.; Brudvig, G. W. *Chem. Rev.* **2006**, *106*, 4455−4483.
(19) Messinger, J.; Renger, G. Photosynthetic Water Splitting. In *Primary Processes of Photosynthesis: Basic Principles and Apparatus*; Renger, G., Ed.; Comprehensive Series in Photochemical and Photobiological Sciences; Royal Society of Chemistry: Cambridge, U.K., in press.
(20) Loll, B.; Kern, J.; Saenger, W.; Zouni, A.; Biesiadka, J. *Nature* **2005**, *438*, 1040−1044.
(21) Yano, J.; Kern, J.; Sauer, K.; Latimer, M. J.; Pushkar, Y.; Biesiadka, J.; Loll, B.; Saenger, W.; Messinger, J.; Zouni, A.; Yachandra, V. K. *Science* **2006**, *314*, 821−825.
(22) DeRose, V. J.; Mukerji, I.; Latimer, M. J.; Yachandra, V. K.; Sauer, K.; Klein, M. P. *J. Am. Chem. Soc.* **1994**, *116*, 5239−5249.
(23) Yachandra, V. K.; Sauer, K.; Klein, M. P. *Chem. Rev.* **1996**, *96*, 2927−2950.
(24) Zouni, A.; Witt, H. T.; Kern, J.; Fromme, P.; Krauss, N.; Saenger, W.; Orth, P. *Nature* **2001**, *409*, 739−743.
(25) Kamiya, N.; Shen, J.-R. *Proc. Natl. Acad. Sci. U.S.A.* **2003**, *100*, 98−103.
(26) Biesiadka, J.; Loll, B.; Kern, J.; Irrgang, K.-D.; Zouni, A. *Phys. Chem. Chem. Phys.* **2004**, *6*, 4733−4736.
(27) Ferreira, K. N.; Iverson, T. M.; Maghlaoui, K.; Barber, J.; Iwata, S. *Science* **2004**, *303*, 1831−1838.
(28) Yano, J.; Kern, J.; Irrgang, K. D.; Latimer, M. J.; Bergmann, U.; Glatzel, P.; Pushkar, Y.; Biesiadka, J.; Loll, B.; Sauer, K.; Messinger, J.; Zouni, A.; Yachandra, V. K. *Proc. Natl. Acad. Sci. U.S.A.* **2005**, *102*, 12047−12052.

1b shows model III with selected amino acid ligands. It should be noted that the amino acid positions are only approximate since they are obtained from the PSII crystal structure[20] and are therefore likely affected by radiation damage.[28]

Understanding the chemistry of photosynthetic water oxidation requires in addition to reliable geometric information also detailed knowledge about the electronic structures of the individual S_n states. An electronic structure describes the oxidation states of the participating ions and the spin couplings between them. In case of the OEC this can be best probed by X-ray techniques such as XANES or RIXS,[29−34] and by modern electron paramagnetic resonance (EPR) techniques. Specifically ^{55}Mn electron nuclear double resonance (ENDOR) has proven to be a very successful tool.[35−40]

EPR signals were obtained for all functional S_n states, except of the short-lived S_4 state[41−49] (for review see ref 50). Among them, the S_2 state produces the strongest signal, the so-called S_2 multiline signal (MLS).[41] For this reason, it was thoroughly studied during the past 25 years, using both conventional cw EPR and pulse EPR techniques. In particular, pulse ^{55}Mn ENDOR and temperature-dependent spin−lattice relaxation measurements were performed.[37,51,52] The S_2 state is known to display, depending on experimental conditions (see below), also an EPR signal at $g = 4.1$ at the expense of the S_2 MLS.[43,44,53]

Many attempts to simulate the EPR and ENDOR spectra and to interpret the EPR-derived magnetic parameters in terms of a structural model of the OEC were undertaken in the past.[37,54−58] Lacking a firm structural basis, all these studies led initially to a large number of possible exchange coupling schemes for the S_2 state. Therefore, the following strategies to reduce the number of possible models were employed: (i) simulation of modified S_2 multiline signals (e.g., by NH_3 binding or Ca^{2+} depletion),[37,55] (ii) explanation of the interconversion of the S_2 MLS into the $g = 4.1$ EPR signal,[37,58] (iii) simultaneous fits of S_2 MLS spectra recorded at different microwave frequencies (Q, X, S band),[54] (iv) simulation of the orientation dependence of the S_2 MLS (data obtained at X-band in one-dimensionally ordered PSII membranes),[59] (v) restriction of parameters to values consistent with those observed in (dimeric) Mn model compounds or in Mn catalase.[55]

Despite intense efforts, largely different geometric and electronic models were proposed on the basis of these previous studies for the Mn_4O_xCa cluster. Based on ^{55}Mn-ENDOR data it is now firmly established that all four Mn ions are magnetically coupled in the S_2 and S_0 states.[37,38,40] Uncertainties remain, however, about the Mn oxidation states. Most of the research groups support the idea that the oxidation state composition of the S_2 state is Mn_4(III,IV,IV,IV) (reviewed in refs 12, 19, 32, and 60). The other option is Mn_4(III, III, III, IV).[55,57,61] Even less is known about the oxidation states of the S_0 state, where the following options are currently viable: Mn_4(II,III,III,III), Mn_4(II,II,III,IV), Mn_4(II,III,IV,IV), and Mn_4(III,III,III,IV).

A promising new way for deriving the oxidation states of the four Mn ions of the OEC and for reducing the number of possible exchange coupling schemes is the combination of reliable information about the geometric structures of different S_n states with corresponding EPR and ^{55}Mn-ENDOR data. The other S_n state, which produces an MLS in the conventional (perpendicular mode) EPR spectroscopy, is the S_0 state.[45−47] This signal is studied in less detail, because it is much weaker than the S_2 MLS and because it is more difficult to prepare samples highly enriched in the S_0 state at the high sample concentrations that are required to perform advanced EPR spectroscopy. Nevertheless, pulse Q-band (34 GHz) EPR and ^{55}Mn-ENDOR spectra of the S_0 state were reported recently.[39,40] In the present work we interpret these results in the framework of the newly available geometric information[21,62] and derive a consistent interpretation for the electronic structures of the S_0 and S_2 states.

All samples in this study contain 3% (v/v) methanol to enhance the hyperfine structure of the S_0 MLS and to avoid the formation of the above-mentioned S_2 state EPR signals at higher g-values. Methanol is known to modify all EPR signals of the

(29) Glatzel, P.; Yano, J.; Bergmann, U.; Visser, H.; Robblee, J. H.; Gu, W. W.; de Groot, F. M. F.; Cramer, S. P.; Yachandra, V. K. *J. Phys. Chem. Solid.* **2005**, *66*, 2163−2167.
(30) Glatzel, P.; Bergmann, U.; Yano, J.; Visser, H.; Robblee, J. H.; Gu, W. W.; de Groot, F. M. F.; Christou, G.; Pecoraro, V. L.; Cramer, S. P.; Yachandra, V. K. *J. Am. Chem. Soc.* **2004**, *126*, 9946−9959.
(31) Yachandra, V. K. *Phil. Trans. R. Soc. London, Ser. B* **2002**, *357*, 1347−1358.
(32) Messinger, J.; Robblee, J. H.; Bergmann, U.; Fernandez, C.; Glatzel, P.; Visser, H.; Cinco, R. M.; McFarlane, K. L.; Bellacchio, E.; Pizarro, S. A.; Cramer, S. P.; Sauer, K.; Klein, M. P.; Yachandra, V. K. *J. Am. Chem. Soc.* **2001**, *123*, 7804−7820.
(33) Haumann, M.; Müller, C.; Liebisch, P.; Iuzzolino, L.; Dittmer, J.; Grabolle, M.; Neisius, T.; Meyer-Klaucke, W.; Dau, H. *Biochemistry* **2005**, *44*, 1894−1908.
(34) Haumann, M.; Liebisch, P.; Müller, C.; Barra, M.; Grabolle, M.; Dau, H. *Science* **2005**, *310*, 1019−1021.
(35) Britt, R. D.; Campbell, K. A.; Peloquin, J. M.; Gilchrist, M. L.; Aznar, C. P.; Dicus, M. M.; Robblee, J.; Messinger, J. *Biochim. Biophys. Acta* **2004**, *1655*, 158−171.
(36) Peloquin, J. M.; Britt, R. D. *Biochim. Biophys. Acta* **2001**, *1503*, 96−111.
(37) Peloquin, J. M.; Campbell, K. A.; Randall, D. W.; Evanchik, M. A.; Pecoraro, V. L.; Armstrong, W. H.; Britt, R. D. *J. Am. Chem. Soc.* **2000**, *122*, 10926−10942.
(38) Kulik, L.; Epel, B.; Messinger, J.; Lubitz, W. *Photosynth. Res.* **2005**, *84*, 347−353.
(39) Kulik, L. V.; Lubitz, W.; Messinger, J. *Biochemistry* **2005**, *44*, 9368−9374.
(40) Kulik, L. V.; Epel, B.; Lubitz, W.; Messinger, J. *J. Am. Chem. Soc.* **2005**, *127*, 2392−2393.
(41) Dismukes, G. C.; Siderer, Y. *Proc. Natl. Acad. Sci. U.S.A.* **1981**, *78*, 274−278.
(42) Hansson, Ö.; Andréasson, L.-E. *Biochim. Biophys. Acta* **1982**, *679*, 261−268.
(43) Casey, J. L.; Sauer, K. *Biochim. Biophys. Acta* **1984**, *767*, 21−28.
(44) Zimmermann, J. L.; Rutherford, A. W. *Biochim. Biophys. Acta* **1984**, *767*, 160−167.
(45) Messinger, J.; Robblee, J. H.; Yu, W. O.; Sauer, K.; Yachandra, V. K.; Klein, M. P. *J. Am. Chem. Soc.* **1997**, *119*, 11349−11350.
(46) Messinger, J.; Nugent, J. H. A.; Evans, M. C. W. *Biochemistry* **1997**, *36*, 11055−11060.
(47) Åhrling, K. A.; Peterson, S.; Styring, S. *Biochemistry* **1997**, *36*, 13148−13152.
(48) Yamauchi, T.; Mino, H.; Matsukawa, T.; Kawamori, A.; Ono, T.-a. *Biochemistry* **1997**, *36*, 7520−7526.
(49) Matsukawa, T.; Mino, H.; Yoneda, D.; Kawamori, A. *Biochemistry* **1999**, *38*, 4072−4077.
(50) Britt, R. D.; Peloquin, J. M.; Campbell, K. A. *Annu. Rev. Biophys. Biomol. Struct.* **2000**, *29*, 463−495.
(51) Lorigan, G. A.; Britt, R. D. *Biochemistry* **1994**, *33*, 12072−12076.
(52) Lorigan, G. A.; Britt, R. D. *Photosynth. Res.* **2000**, *66*, 189−198.
(53) Boussac, A.; Kuhl, H.; Un, S.; Rögner, M.; Rutherford, A. W. *Biochemistry* **1998**, *37*, 8995−9000.
(54) Åhrling, K. A.; Pace, R. J. *Biophys. J.* **1995**, *68*, 2081−2090.
(55) Zheng, M.; Dismukes, G. C. *Inorg. Chem.* **1996**, *35*, 3307−3319.
(56) Hasegawa, K.; Ono, T.-A.; Inoue, Y.; Kusunoki, M. *Chem. Phys. Lett.* **1999**, *300*, 9−19.
(57) Carell, T. G.; Tyryshkin, A. M.; Dismukes, G. C. *J. Biol. Inorg. Chem.* **2002**, *7*, 2−22.
(58) Charlot, M. F.; Boussac, A.; Blondin, G. *Biochim. Biophys. Acta* **2005**, *1708*, 120−132.
(59) Hasegawa, K.; Kusunoki, M.; Inoue, Y.; Ono, T.-A. *Biochemistry* **1998**, *37*, 9457−9465.
(60) Messinger, J. *Phys. Chem. Chem. Phys.* **2004**, *6*, 4764−4771.
(61) Kuzek, D.; Pace, R. J. *Biochim. Biophys. Acta* **2001**, *1503*, 123−137.
(62) Robblee, J. H.; Messinger, J.; Cinco, R. M.; McFarlane, K. L.; Fernandez, C.; Pizarro, S. A.; Sauer, K.; Yachandra, V. K. *J. Am. Chem. Soc.* **2002**, *124*, 7459−7471.

Mn_4O_xCa cluster,[45,46,48,49,52,63−70] and direct binding to the cluster was demonstrated in the S_2 state by ESEEM spectroscopy.[71−74] While methanol is clearly affecting the coupling between the Mn ions, no evidence exists as yet that it changes the overall oxidation states in the Mn_4O_xCa cluster. The possibility that methanol binding is causing a significant structural change that alters the Mn−Mn distances is highly unlikely since EXAFS measurements of the S_1 state[22,75] and the S_0 state[33,62] yield basically identical results with and without 3% methanol, respectively. In addition, the overall oxygen evolution rate is basically unaffected by the addition of 3% methanol.[47,74]

Experimental Section

Sample Preparation. PSII membranes were prepared according to standard procedures[45] and washed several times after the Triton treatment for complete starch removal. S_2 state samples were obtained by concentrating dark-adapted PSII membranes containing 250 μM PPBQ (phenyl-*p*-benzoquinone) and 1 mM EDTA in 3 mm outer diameter (Q-band) quartz tubes by centrifugation (~25 mg of chlorophyll/mL final concentration) and subsequent illumination at 200 K. S_0 state samples were prepared using the 3-flash/FCCP approach described previously.[45,62] The samples were finally concentrated by centrifugation in Q-band EPR tubes. After completing the ^{55}Mn-ENDOR experiments the S_0 state population was determined to be 65(±5) % (the rest being S_1) by the amplitude of the S_2 EPR multiline signal generated by 200 K illumination compared to that of S_2 control samples. All samples contained 3% (v/v) methanol in order to (i) obtain maximal S_2 MLS amplitudes by avoiding $g = 4.1$ signal formation and (ii) allow the observation of the S_0 EPR multiline signal.[46]

Pulse EPR Spectroscopy. The experiments were performed using a Bruker Elexsys-580 Q-band pulse EPR spectrometer, which was equipped with a home-built cylindrical resonator[76] and an Oxford ITC-5025 helium flow temperature controller and CF935 cryostat. The sample temperature was 4.5 K. X-band pulse EPR experiments were performed with a Bruker ESP-380E spectrometer equipped with a dielectric ring resonator, temperature controller, and an Oxford ITC liquid helium flow system.

For recording field-swept echo (FSE) EPR spectra the two-pulse sequence "$\pi/2-\tau-\pi-\tau-$echo" was used, with a 64 ns π-pulse and $\tau = 260$ ns. The pulse sequence repetition time was 1 ms for the S_2 state and 12 μs for the S_0 state.

The pulse ^{55}Mn-ENDOR experiments were performed using SpecMan control software that varies the radio frequency (RF) randomly in the desired range.[77] This leads to a decrease of the RF-induced heat accumulation in the resonator and in turn to a reduction of heating artifacts. The Davies-ENDOR pulse sequence ($\pi-T-\pi/2-\tau-\pi-\tau-$echo) was used with a radio frequency π-pulse duration of 5 μs for the S_2 state and 4 μs for the S_0 state. In all measurements the S_1 background signal was subtracted that was obtained separately on parallel samples.

Theory and Computation. In this section we briefly summarize the theoretical basis for the analysis of the EPR and ENDOR data of the Mn_4O_xCa cluster. The spin-Hamiltonian of a system with *n* coupled Mn ions is

$$H = \sum_i \beta B_0 \cdot g_i \cdot S_i + \sum_i S_i \cdot a_i \cdot I_i + \sum_i S_i \cdot D_i \cdot S_i - \sum_{i<k} J_{ik}(S_i S_k) \quad (1)$$

Here the indices i and k run from A to D (the four Mn ions), β is the Bohr magneton, g_i is the g-matrix for the electron spin of the i-th Mn ion, S_i and I_i are the operators of the electron spin and nuclear spin of the i-th Mn ion, respectively, a_i is the tensor of hyperfine interaction (HFI) for the i-th Mn ion, D_i is the zero-field splitting (ZFS) tensor for the electron spin of the i-th Mn ion, J_{ik} is the exchange coupling constant (the strength of the exchange coupling) between the i-th and k-th Mn ions, and • denotes matrix multiplication. The nuclear Zeeman interactions, the nuclear quadrupole interactions (NQI) for the Mn nuclei, and the ZFS between electron spins at different Mn ions are not included in the spin-Hamiltonian. In this notation a negative value of the exchange coupling constant corresponds to antiferromagnetic exchange interaction. The individual electron spins S_i of the Mn(II), Mn(III), and Mn(IV) ions are assumed to be high spin, i.e., $^5/_2$, 2, and $^3/_2$, respectively.

The application of this Hamiltonian requires that the spins are trapped on the four Mn ions in the S_0 and S_2 states; i.e., spin delocalization between the Mn ions and onto the ligands is negligible. This assumption is valid for the great majority of the synthetic Mn complexes,[78] and there is no evidence that it is invalid for the S_0 and S_2 states of the OEC. For the S_1 state charge delocalization was suggested recently on the basis of resonant inelastic X-ray scattering (RIXS) measurements.[30] It should be pointed out that charge delocalization does not necessarily imply that also the spins of the four Mn ions are delocalized.

Calculation of the Energy Separation Δ between Ground and First Excited State. Usually, the exchange interaction term

$$H_{ex} = -\sum_{i<k} J_{ik}(S_i S_k) \quad (2)$$

is much greater than the other terms in eq 1. In this case, the exchange interaction effectively couples the individual electron spins at different Mn ions. Therefore, an effective electron spin with the operator

$$S_T = \sum_i S_i \quad (3)$$

can be used, which greatly simplifies eq 1 (see eqs 4 and 9). In this case also the energy levels of the system determined by eq 1 can be grouped into multiplets (so-called "exchange multiplets"). The energy difference between different multiplets is determined by the exchange interaction term H_{ex} (eq 2). Equation 2 therefore allows calculating the energy difference Δ between the ground and first excited-state multiplets. For this the energy difference between the centers of gravity of the two spin multiplets with the lowest energies was determined and compared to the experimental values of 21 cm^{-1} (S_0 state)[39] and 35 cm^{-1} (S_2 state).[51,70,79]

Simulation of EPR and ENDOR Spectra. Within each multiplet all levels have the same value S_T of the effective electron spin and can be treated as Zeeman levels with effective spin S_T. For $S_T = {}^1/_2$ the

(63) Su, J. H.; Havelius, K. G. V.; Mamedov, F.; Ho, F. M.; Styring, S. *Biochemistry* **2006**, *45*, 7617−7627.
(64) Ioannidis, N.; Zahariou, G.; Petrouleas, V. *Biochemistry* **2006**, *45*, 6252−6259.
(65) Åhrling, K. A.; Evans, M. C. W.; Nugent, J. H. A.; Pace, R. J. *Biochim. Biophys. Acta* **2004**, *1656*, 66−77.
(66) Ioannidis, N.; Petrouleas, V. *Biochemistry* **2000**, *39*, 5246−5254.
(67) Deák, Z.; Peterson, S.; Geijer, P.; Åhrling, K. A.; Styring, S. *Biochim. Biophys. Acta* **1999**, *1412*, 240−249.
(68) Boussac, A.; Kuhl, H.; Ghibaudi, E.; Rögner, M.; Rutherford, A. W. *Biochemistry* **1999**, *38*, 11942−11948.
(69) Boussac, A.; Deligiannakis, Y.; Rutherford, A. W. Effects of Methanol on the Mn_4-Cluster of Photosystem 2. In *Photosynthesis: Mechanisms and Effects*; Garab, G., Ed.; Kluwer: Dordrecht, 1998; Vol. II, pp 1233−1240.
(70) Pace, R. J.; Smith, P.; Bramley, R.; Stehlik, D. *Biochim. Biophys. Acta* **1991**, *1058*, 161−170.
(71) Åhrling, K. A.; Evans, M. C. W.; Nugent, J. H. A.; Ball, R. J.; Pace, R. J. *Biochemistry* **2006**, *45*, 7069−7082.
(72) Evans, M. C. W.; Ball, R. J.; Nugent, J. H. A. *FEBS Lett.* **2005**, *579*, 3081−3084.
(73) Evans, M. C. W.; Gourovskaya, K.; Nugent, J. H. A. *FEBS Lett.* **1999**, *450*, 285−288.
(74) Force, D. A.; Randall, D. W.; Lorigan, G. A.; Clemens, K. L.; Britt, R. D. *J. Am. Chem. Soc.* **1998**, *120*, 13321−13333.
(75) Robblee, J. H.; Cinco, R. M.; Yachandra, V. K. *Biochim. Biophys. Acta* **2001**, *1503*, 7−23.
(76) Sinnecker, S.; Reijerse, E.; Neese, F.; Lubitz, W. *J. Am. Chem. Soc.* **2004**, *126*, 3280−3290.
(77) Epel, B.; Gromov, I.; Stoll, S.; Schweiger, A.; Goldfarb, D. *Concepts Magn. Reson., Part B* **2005**, *26*, 36−45.
(78) Mukhopadhyay, S.; Mandal, S. K.; Bhaduri, S.; Armstrong, W. H. *Chem. Rev.* **2004**, *104*, 3981−4026.
(79) Hansson, Ö.; Aasa, R.; Vänngård, T. *Biophys. J.* **1987**, *51*, 825−832.

exchange multiplet consists of two levels that are separated by Zeeman interactions, which can be treated as an effective Kramer's doublet. This energy difference between these two levels of one multiplet is small (0.3 cm^{-1} at X-band and 1.1 cm^{-1} at Q-band) compared to the separation between multiplets.

For the case of two coupled ions, the value of S_T completely characterizes the multiplet. When more than two ions couple, the situation is more complicated and several multiplets may have the same S_T value. In this case the multiplets differ in the mutual ordering of the individual electron spins.

The spin-Hamiltonian (eq 1) can be rewritten in the coupled representation *for each exchange multiplet* (here the constant contribution of H_{ex} (eq 2) is not included):

$$H = \beta B_0 \cdot g \cdot S_T + \sum_i (S_T \cdot A_i \cdot I_i) + S_T \cdot D_T \cdot S_T \qquad (4)$$

where g is the effective g-matrix. The experimentally determined effective HFI tensors, A_i, for the Mn nuclei are related to the intrinsic hyperfine tensors a_i via the projection matrices ρ_i:

$$A_i = \rho_i \cdot a_i \qquad (5)$$

The values of ρ_i are different for each exchange multiplet. They are determined by the values of the electron spin S_i of the individual Mn ions, the strength of the exchange couplings between them J_{ik}, the strength of the ZFS interaction D_i, and the value of the total spin:

$$\rho_i = \rho_i(S_i, J_{ik}, D_i, S_T) \qquad (6)$$

More precisely, ρ_i depends on the ratio of J_i and D_i relative to one specific energy parameter, generally taken as one of the exchange constants.

The effective ZFS term $H_{ZFS} = S_T \cdot D_T \cdot S_T$ vanishes in eq 4, if a ground state multiplet with $S_T = {}^1/_2$ is considered.[39,51,79−81] Accordingly, eq 7 was used for simulating the EPR spectra:

$$H = \beta B_0 \cdot g \cdot S_T + \sum_i (S_T \cdot A_i \cdot I_i) \qquad (7)$$

For simulating the ENDOR spectra the nuclear Zeeman term $H_{NZ} = \sum_i \gamma_N(B_0 I_i)$ was added to eq 7, where γ_N is the Mn nuclear gyromagnetic ratio.

Second-order perturbation theory was used to calculate EPR and ^{55}Mn-ENDOR spectra. Gaussian inhomogeneous broadening of the electron and nuclear spin transitions was assumed. In order to obtain the presented values several cycles of sequential fits of the EPR and ^{55}Mn-ENDOR spectra were performed.

Calculation of Spin Projection Matrices. In general ρ_i is a 3×3 matrix. This matrix can be reduced to scalar, when there is no ZFS in the system, i.e., if all D_i tensors are zero. The anisotropy of ρ_i appears because ZFS interactions introduce perturbations to the ordering of the electron spins of individual ions via exchange interaction. In the simple case of two coupled ions the amplitude of this perturbation depends on the ratio of ZFS strength, which is anisotropic, to the strength of the exchange interaction. This means that the effective HFI tensor of a Mn nucleus may be anisotropic, even if its intrinsic HFI tensor is isotropic (so-called "transfer of hyperfine anisotropy").[82,83] For the complicated case of more than two ions the extent of this effect is determined mainly by the relation between the strength of the ZFS and the energy difference between the exchange multiplets. When the former is much weaker than the latter, the anisotropy of ρ_i can be neglected, and this is what we assume for our analysis (see Discussion).

For the case of ρ_i being proportional to the identity matrix, which occurs in the absence of ZFS, the isotropic parts of the effective and the intrinsic HFI constants, $A_{i,iso}$ and $a_{i,iso}$, are related by the scalar $\rho_{i,iso}$ (isotropic part of the projection matrix; compare to eq 5):

$$A_{i,iso} = \rho_{i,iso} a_{i,iso} \qquad (8)$$

For the case that both ρ_i and a_i are anisotropic, eq 8 is no longer valid. The degree of deviation depends on (i) the relation between the strength of ZFS and the exchange couplings and (ii) the degree of the anisotropy of a_i.

Similar to a previous attempt,[58] we base our general analysis on eq 8, and possible deviations are then considered on the basis of specific models in the Discussion section. Accordingly, the following simplified spin Hamiltonian was employed for calculating the projection matrices:

$$H = g_e \beta B_0 S_{T,z} - \sum_{i<k} J_{ik}(S_i S_k) \qquad (9)$$

where

$$S_{T,z} = \sum_i S_{i,z}$$

is the z-component of the total electronic spin and g_e is the free electron g-value.

The eigenstates of this Hamiltonian (eq 9) were obtained by full diagonalization. The eigenstate with the lowest energy was assumed to belong to the lowest exchange multiplet, i.e., to represent the ground state of the spin system. The projection matrices for the ground state were determined by the relation (see ref 55 for a similar expression):

$$\rho_{i,iso} = \frac{\langle (S_i S_T) \rangle}{\langle S_T^2 \rangle} \qquad (10)$$

where the brackets denote quantum-mechanical averaging of the operators over the eigenstate with the lowest energy. The effective spin of the ground state S_T was determined from the relation:

$$\langle S_T^2 \rangle = S_T(S_T + 1) \qquad (11)$$

Numerical calculations were performed using Maltab 6.5 software and the EasySpin 2.0.3 package.[84]

Search Protocol for Possible Mn Oxidation States of the S_0 and S_2 States. The general search for possible oxidation states of the S_0 and S_2 states was initially carried out with exchange coupling constants that were varied in arbitrary units (au), which we denote by j_{ik}. The true values of the exchange coupling constants J_{ik} in cm^{-1} are obtained from the corresponding j_{ik} values by scaling to the experimentally determined energy separations Δ between the ground state and the first excited state by employing eq 2.

In all calculations three exchange couplings, namely j_{AB}, j_{BD}, and j_{CD}, were varied independently in the range between -30 and $+6$ au, while j_{BC} was fixed to -10 au. This is possible, since at this stage only the relative values of the exchange coupling constants are important. The negative sign of j_{BC} excludes models with ferromagnetic coupling between Mn_B and Mn_C and thereby helps to establish the $S = {}^1/_2$ ground state. For the general search the step width was either 1.5 au or 3.0 au, while it was 1.0 au or 2.0 au during the detailed searches. For each set of Mn oxidation states all possible permutations of Mn ions in different oxidation states were calculated. For example, for the

(80) Britt, R. D.; Lorigan, G. A.; Sauer, K.; Klein, M. P.; Zimmermann, J.-L. *Biochim. Biophys. Acta* **1992**, *1040*, 95−1001.
(81) Åhrling, K. A.; Peterson, S.; Styring, S. The S_0 state EPR signal from the Mn cluster arises from an isolated ground state. In *Photosynthesis: Mechanisms and Effects*; Garab, G., Ed.; Kluwer Academic Publishers: Dordrecht, 1998; Vol. 2, pp 1291−1294.
(82) Zheng, M.; Khangulov, S. V.; Dismukes, G. C.; Barynin, V. V. *Inorg. Chem.* **1994**, *33*, 382−387.
(83) Schäfer, K.-O.; Bittl, R.; Zweygart, W.; Lendzian, F.; Haselhorst, G.; Weyhermüller, T.; Wieghardt, K.; Lubitz, W. *J. Am. Chem. Soc.* **1998**, *120*, 13104−13120.
(84) Stoll, S.; Schweiger, A. *J. Magn. Reson.* **2006**, *178*, 42−55.

Mn_4(III,III,III,IV) oxidation state the four cases were analyzed, in which the Mn(IV) ion is in all possible positions (A−D; Figure 1c).

Validation of Spin Coupling Models. Numerical solutions with $S_T = {}^1/_2$ obtained with the above equations for J_{ik} (eq 2) and for A_i (eq 8) are compared to ranges of values known from model systems. If the obtained numbers do not fall into the ranges specified below, the result was considered invalid and was rejected.

I. The spin topology is considered valid if all four experimental $A_{i,\mathrm{iso}}$ values are reproduced by the absolute value of the calculated effective ^{55}Mn−HFI constant $A_{i,\mathrm{calcd}} = \rho_{i,\mathrm{iso}} a_{i,\mathrm{iso}}$ with 10% precision. This takes into account (i) the uncertainty of the determination of $A_{i,\mathrm{iso}}$, (ii) possible deviations from eq 8 due to ZFS effects, and (iii) the possible deviation of the $a_{i,\mathrm{iso}}$ value of the OEC from that of the dimanganese catalase, which we take as 237 MHz for Mn(IV), 192 MHz for Mn(III), and 253 MHz for Mn(II).[82] This will be referred to in the text as Constraint I.

II. The reported limits of precedented values of the exchange coupling constants are as follows: −20 to +10 cm^{-1} for the Mn(II)−Mn(II) pair; −40 to +20 cm^{-1} for Mn(II)−Mn(III) and Mn(II)−Mn(IV) pairs; −240 to +100 cm^{-1} for the Mn(III)−Mn(III) pair.[78,85,86] For di-μ-oxo bridged Mn(III)−Mn(IV) and Mn(IV)−Mn(IV) pairs a strong antiferromagnetic coupling in the range −250 to −150 cm^{-1} is usually found. For other types of bridging between Mn(III)−Mn(IV) and Mn(IV)−Mn(IV) the interaction is usually weaker. The magnitude of such couplings strongly depends on the bond geometry and the type of bridging. Both weakly ferromagnetic and antiferromagnetic couplings on the order of several tens of wave numbers have been reported.[78,85] The application of this criterion is soft and model dependent, so that it will be further discussed in the text, where it is referred to as Constraint II. One exception from this rule is a linear mono-μ-oxo bridge, for which strong antiferromagnetic coupling in the range of −350 cm^{-1} to −200 cm^{-1} is typical.[78] However, EXAFS measurements on the Mn_4O_xCa cluster do not provide any evidence for this bridging mode.

To filter out from the remaining solutions the electronic structures that most accurately describe the Mn_4O_xCa cluster in redox states S_0 and S_2 we applied two further constraints:

III. On the basis of the new structural information about the Mn_4O_xCa cluster obtained by single-crystal EXAFS we employ a "T2(S_2) structure filter" (T2(S_2)-SF) for the S_2 state, i.e., $|J_{AB}| > |J_{BC}| \approx |J_{CD}| > |J_{BD}|$ with the following absolute limits: $-250\ cm^{-1} \le J_{AB} \le -100\ cm^{-1}$; $-100\ cm^{-1} \le J_{BC}, J_{CD} \le -20\ cm^{-1}$; $-20\ cm^{-1} \le J_{BD} \le +20\ cm^{-1}$. For the S_0 state a slightly modified structure filter (T2(S_0)-SF) was employed with $-250\ cm^{-1} \le J_{AB} \le +10\ cm^{-1}$ (all other limits are the same). These structure filters are explained in detail later in the text (Constraint III).

IV. For a final selection also recent FTIR data on mutants around the Mn_4O_xCa cluster and the requirement of consistent solutions for electronic structures of the S_0 and S_2 states (taking into account known structural changes) were employed (Constraint IV).

Flow diagrams of the analysis procedure are provided in the Supporting Information (FD1 to FD4).

Results

Determination of the Effective Hyperfine Interaction Parameters A_i of the S_0 and S_2 States. As outlined in the theory section, the reliable determination of the effective hyperfine interaction parameter, A_i, for the individual Mn ions (Mn_A, Mn_B, Mn_C, Mn_D) forms the basis for the elucidation of the electronic structure of the S_0 and S_2 states. The first step in this direction was done in our previous paper,[40] where ^{55}Mn-ENDOR spectra for the S_2 and S_0 states were simulated under the following assumptions: (i) the g-matrix and ^{55}Mn HFI-tensors are axially symmetric; (ii) the axis of the axial symmetry coincides for all g matrices and A_i tensors; (iii) the influence of nuclear quadrupole interactions (NQI) is negligible; i.e., the NQI tensors of all Mn nuclei are zero. With these assumptions it was possible to obtain quite good simulations of the ^{55}Mn-ENDOR spectra for the S_2 and S_0 states. However, the simulation of the EPR spectra turned out to be problematic. This implies that the above assumptions impose too strict constraints on the simulation parameters. Therefore, a refinement of the parameters was performed by simultaneous constrained simulations of the Q-band EPR and ^{55}Mn-ENDOR spectra for the S_2 and S_0 states and of X-band ^{55}Mn-ENDOR spectra in case of the S_2 state.

Table 1. Principal Values of the Effective g-Matrix and the ^{55}Mn-HFI Tensors for the S_2 State[a]

	g	A_1, MHz	A_2, MHz	A_3, MHz	A_4, MHz	model
x	1.997[e]	310	235	185	170	this work[b]
y	1.970[e]	310	235	185	170	
z	1.965[e]	275	275	245	240	
iso[c]	1.977	298	248	205	193	
aniso[d]	0.032	35	40	60	70	
x	1.989	329	287	243	218	ref 58
y	1.987	305	254	258	188	
z	1.977	339	224	213	167	
iso[c]	1.984	324	255	238	191	
aniso[d]	0.012	34	63	45	51	
⊥	1.97	311	232	200	180	ref 37[f]
∥	1.99	270	270	250	240	
iso[c]	1.977	297	245	217	200	
aniso[d]	0.02	41	38	50	60	

[a] The sign of the effective principal HFI values was not determined in this study, and therefore absolute values are provided. [b] The line width of the EPR transitions was taken to be 2.5 mT (fwhh), and that of the ^{55}Mn-ENDOR transitions, to be 7 MHz (fwhh). [c] The isotropic g and A_i (i = 1−4) values are the numerical averages of the individual values: $g_{\mathrm{iso}} = (g_x + g_y + g_z)/3$ and $A_{\mathrm{iso}} = (A_{i,x} + A_{i,y} + A_{i,z})/3$. In the case of axial tensors the x and y values both equal the perpendicular component, i.e., for example, $g_{\mathrm{iso}} = (2g_\perp + g_{\parallel})/3$. [d] The anisotropy in the g and A_i (i = 1−4) values is expressed as the difference between the largest and the smallest component of the axial or rhombic tensors. [e] Values adopted from ref 87. [f] Peloquin et al. additionally assumed quadrupole splittings on the order of −3 to +8 MHz. For simulations (see Supporting Information) these have been taken into account.

S_2 State. In order to refine our Q-band S_2 EPR spectra simulations we employed the recently published g_x-, g_y-, and g_z-values that were derived from W-band spectra of PSII single crystals;[87] i.e., we lifted the restriction of an axial g-matrix. As starting values we used our previously obtained axial ^{55}Mn-HFI tensors. In order to keep the number of free parameters to a minimum we maintained all other restrictions. Only slight variations of the original ^{55}Mn-HFI parameters by 0−10 MHz were required (Table 1) to obtain excellent agreement between the experimental echo detected EPR spectrum (and its derivative; black lines in Figure 2) and the simulation (red lines; Figure 2). Variation of the g-values did not lead to an appreciable improvement. For comparison, Table 1 lists two previously published parameter sets for the methanol-treated S_2 state, which are based on X-band ^{55}Mn-ENDOR[37] and EPR[37,58] measurements. Simulations of the new Q-band data with these parameter sets are less satisfactory and are shown in Figure S1 of the Supporting Information.

(85) Hasegawa, K.; Ono, T.-A.; Inoue, Y.; Kusunoki, M. *Bull. Chem. Soc. Jpn.* **1999**, *72*, 1013−1023.
(86) Mukherjee, C.; Weyhermüller, T.; Wieghardt, K.; Chaudhuri, P. *Dalton Trans.* **2006**, 2169−2171.
(87) Teutloff, C.; Kessen, S.; Kern, J.; Zouni, A.; Bittl, R. *FEBS Lett.* **2006**, *580*, 3605−3609.

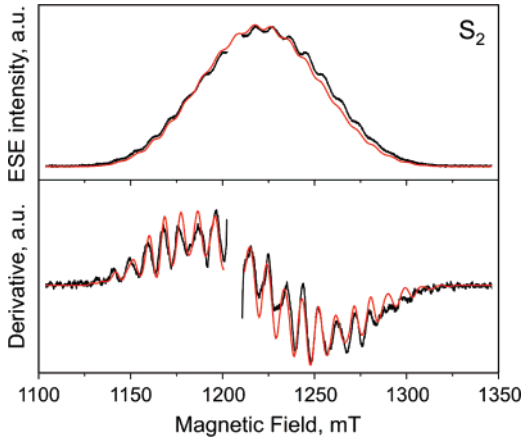

Figure 2. Upper panel: Echo-detected EPR spectrum of the S_2 state (black solid line) in photosystem II membrane fragments (BBY) containing 3% methanol and its simulation (red solid line) according to the parameters derived in this work (top part of Table 1). Simulations using previously derived parameter sets are presented in the Supporting Information (Figure S1). Experimental conditions: temperature 4.5 K, microwave frequency $\nu_{mw} = 33.85$ GHz (for further details see Experimental Section). Lower panel: CW EPR-like derivative spectra obtained by the numerical pseudo-modulation of the corresponding spectra from the upper panel. An amplitude of 2 mT was employed for the pseudomodulation.

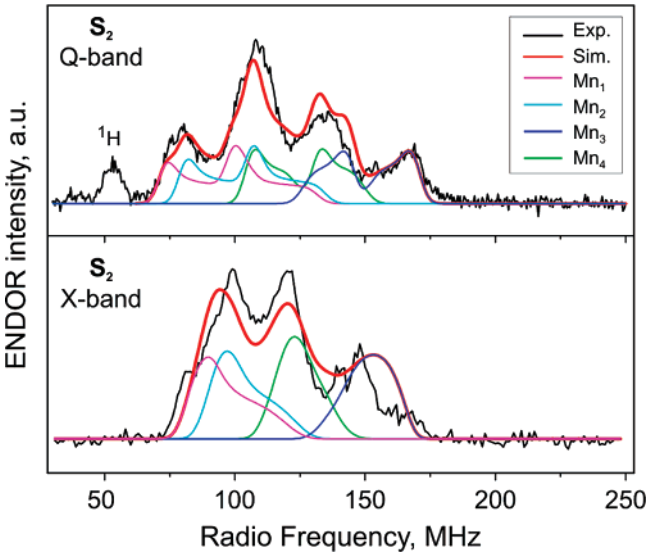

Figure 3. Pulse ^{55}Mn-ENDOR spectra at Q-band (top) and X-band (bottom) of the S_2 state (black solid line) and their simulations (red lines) according to the parameters derived in this study (see top part of Table 1). The contributions of the individual Mn ions are shown in different colors. Here the Mn ions are labeled Mn_1, Mn_2, Mn_3, and Mn_4, because at this stage no unique assignment to Mn_A, Mn_B, Mn_C, and Mn_D in Figure 1c can be made. Experimental conditions: Temperature 4.5 K, microwave frequency $\nu_{mw} = 33.85$ GHz, magnetic field $B_0 = 1260$ mT for Q-band; and Temperature 4.2 K, microwave frequency $\nu_{mw} = 9.71$ GHz, magnetic field $B_0 = 360$ mT for X-band.

Simulations (red lines) of the experimental Q-band (top) and X-band (bottom) ^{55}Mn-ENDOR spectra (black lines) using these refined parameters (Table 1, top) are shown in Figure 3. The contributions of the individual Mn ions to the ^{55}Mn-ENDOR spectra are indicated by differently colored lines. As expected from the minor variation in the HFI parameters (Table 1) this new Q-band simulation (Figure 3; thick red line) is almost identical to our previous one that was obtained on the basis of axial g-matrices.[40] This shows that the simulation of ^{55}Mn-ENDOR spectra results in a very reliable determination of the

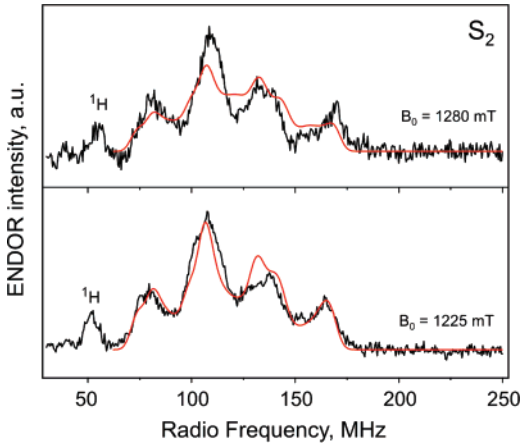

Figure 4. Pulse ^{55}Mn-ENDOR spectra of the S_2 state (black solid lines), measured at different values of the magnetic field B_0 and their simulations according to the parameters listed in Table 1 (this work). Upper panel: $B_0 = 1280$ mT. Lower panel: $B_0 = 1225$ mT. The other experimental parameters are the same as those in Figure 3.

effective HFI values of the Mn ions. This is further supported by the satisfactory agreement between simulation and experimental data that is reached with these parameters at two further magnetic field values B_0 (Figure 4). A comparison of our Q-band ^{55}Mn-ENDOR spectrum with previous simulations is given in the Supporting Information (Figure S2).

S_0 State. No precise g-values are available at present for the S_0 state from high-field EPR experiments. Therefore, simulations of the Q-band S_0 state EPR signal were performed employing a rhombic g-matrix that had a principal axis (z-axis) that coincides with the principal axis (z-axes) of the four axial ^{55}Mn-HFI tensors. During the simulations only the principal g-values g_x, g_y, and g_z were varied, while the ^{55}Mn-HFI values were fixed to the previously determined axial HFI tensor.[40] This procedure appears justified, since (i) it significantly reduces the number of variable parameters and (ii) only minor variations of the HFI parameters are expected on the basis of the above S_2 state simulations.

The results are summarized in Table 2, and the experimental (black) and calculated (red) EPR spectra for the S_0 state are displayed in Figure 5. The general shape of the spectrum is well reproduced for both the ESE-detected and the derivative spectrum. However, the wing at the high-field edge cannot be satisfactorily simulated in the framework of the assumed model.

Our simulation of the S_0 EPR spectrum results in a large g-anisotropy. Since the simulation of the S_0 state spectrum is not perfect, we consider our values as preliminary. However, such a large g-anisotropy is not unreasonable when taking into account (i) the small value of the energy separation to the first excited state[39] and (ii) the suggested presence of three Mn(III) ions in the S_0 state (see below), which might exhibit a strong ZFS due to Jahn−Teller distortions.

Figure 6 presents the simulation of the ^{55}Mn-ENDOR spectra for the S_0 state for two different B_0 values with the parameters listed in Table 2 (top). The major spectral features are well reproduced by the simulation, but some deviations remain. These discrepancies may (i) be due to nuclear quadrupole interactions (NQI's), which are neglected in the present simulation or (ii) arise from a deviation of the ^{55}Mn-HFI tensors from axial

Table 2. Principal Values of the Effective *g*-Matrix and the ^{55}Mn-HFI Tensors for the S_0 State[a]

	g	A_1, MHz	A_2, MHz	A_3, MHz	A_4, MHz	model
x	2.009	320	270	190	170	this work[b]
y	1.855	320	270	190	170	
z	1.974	400	200	280	240	
iso[d]	1.946	347	247	220	193	
aniso[e]	0.154	80	70	90	70	
x	1.9557	316	226	206	195	ref 88[c]
y	1.9578	326	233	231	195	
z	2.0530	385	276	184	195	
iso[d]	1.9888	342	245	207	195	
aniso[e]	0.0973	69	50	47	0	

[a] The sign of the effective principal HFI values was not determined in this study, and therefore absolute values are provided. [b] The line width of the EPR transitions was taken to be 4.2 mT (fwhh), and that of the ^{55}Mn-ENDOR transitions, to be 7 MHz (fwhh). [c] The principal values of ^{55}Mn-HFI tensors of Kusunoki (MHz) were converted from the corresponding values in Gauss given by Kusunoki[88] using a *g*-value of $g = 2$ for conversion. Slight non-collinearity of *g* and Mn-HFI tensors was suggested by Kusunoki.[88] This has been taken into account for the fits presented in Figures S3 and S4. [d] The isotropic *g* and A_i ($i = 1-4$) values are the numerical average of the individual values: $g_{iso} = (g_x + g_y + g_z)/3$ and $A_{iso} = (A_{i,x} + A_{i,y} + A_{i,z})/3$. [e] The anisotropy in the *g* and A_i ($i = 1-4$) values is expressed as the difference between the largest and the smallest component of the tensor.

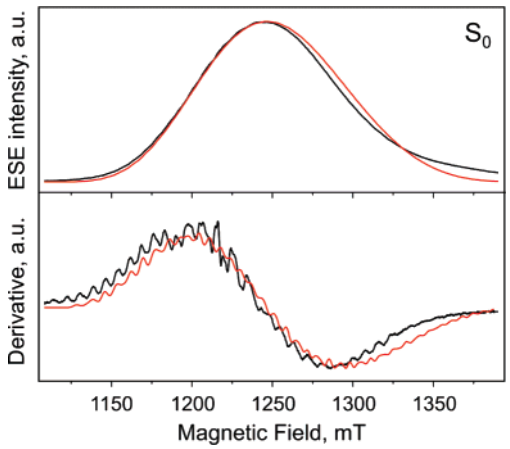

Figure 5. Upper panel: Echo-detected EPR spectrum of the S_0 state of PSII membranes containing 3% methanol (black solid line) and its simulation (red solid line) according to the parameters listed in Table 2 (this work). Temperature 4.5 K, microwave frequency $\nu_{mw} = 34.123$ GHz. Lower panel: CW EPR-like derivative spectra obtained by numerical pseudo-modulation of the corresponding spectra from the upper panel. An amplitude of 2 mT was employed for the pseudomodulation.

symmetry. Nevertheless, Figures 5 and 6 indicate that the ^{55}Mn-HFI tensors (A_i) of Table 2 are reliable. Comparisons of our experimental spectra to less satisfying simulations with parameters previously derived by Kusunoki[88] (Table 2; bottom) are presented in the Supporting Information (Figures S3 and S4).

It is important to note that for the elucidation of the electronic structures we rely in the following only on the precision of the derived ^{55}Mn-HFI's (A_i values). During fitting we allow a deviation of up to 10% between the calculated (see below) and the fitted isotropic HFI values (Tables 1 and 2), which also accounts for possible deviations of the intrinsic isotropic HFI values, a_i, from those reported for Mn catalase (see below).

(88) Kusunoki, M. Simulation of the "S_0-state" EPR signal from the Mn cluster in photosystem II. Evidence for a piece of a thermally accessible O_2-binding state. In *12th International Congress on Photosynthesis*; CSIRO Publishing: Collingwood, Australia, 2001; pp S13−008.

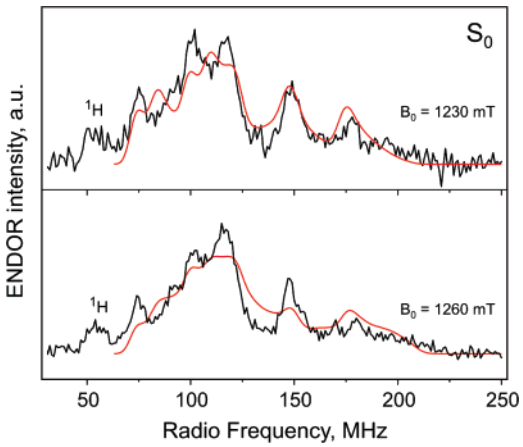

Figure 6. Pulse ^{55}Mn-ENDOR spectra of the S_0 state (black solid lines), measured at two different magnetic field positions B_0, and their simulations (red solid lines) according to the parameters listed in Table 2 (this work). Microwave frequency $\nu_{mw} = 33.83$ GHz. Upper panel: $B_0 = 1230$ mT. Lower panel: $B_0 = 1260$ mT. The other experimental parameters are listed in the text.

Therefore, a more precise simulation of the experimental spectra employing additional free parameters is not required at this point.

General Search for Mn Oxidation States of the S_0 and S_2 States. In this general search for Mn oxidation states of the S_0 and S_2 states of the OEC, we test the compatibility of different coupling schemes with (i) the effective ^{55}Mn-HFI values (A_i) of the S_0 and S_2 states and (ii) the range of possible exchange coupling constants, J_{ik} (Constraints I and II).

The general coupling scheme used in this study to analyze the electronic structure of the OEC is shown in Figure 1c, right side. The Mn and oxygen ions are shown schematically in a projection along the membrane normal as large and small filled circles, respectively. The red lines connect Mn ions for which exchange coupling of their electrons is assumed. The strength of the exchange coupling, J_{ik}, is a function of the number, type, and geometry of the bridges between the Mn ions. In general it can be expected that bis-μ-oxo bridged units have a stronger exchange coupling than mono-μ-oxo bridged ones. Similarly, the coupling will be weakened if one of the bridges in a bis-μ-oxo bridged unit is protonated or forms a μ_3-bridge with a third partner. Accordingly, we expect for example that the strength of the antiferromagnetic exchange couplings J_{ik} for the specific structural model shown in Figure 1c, left side, follows the order $|J_{AB}| > |J_{BC}| \approx |J_{CD}| > |J_{BD}|$. Ca is not part of the coupling scheme, since Mn−Mn couplings via Ca are expected to be negligibly small. The general outline of this coupling scheme is similar to that used previously by Charlot and co-workers.[58]

Figure 7 shows exchange coupling schemes that were derived as described above for suggested models of the Mn_4O_xCa cluster. The coupling schemes are grouped into three categories: dimer of dimers (DOD), trimer−monomers (TrM), and tetramers (T). The red dots in Figure 7 represent the Mn ions, and the strength of the Mn−Mn couplings are coded by the type of lines connecting them. Strong antiferromagnetic couplings are represented by a double line, medium strength antiferromagnetic couplings are represented by a single solid line, and weak antiferro- or ferromagnetic couplings are marked by dashed

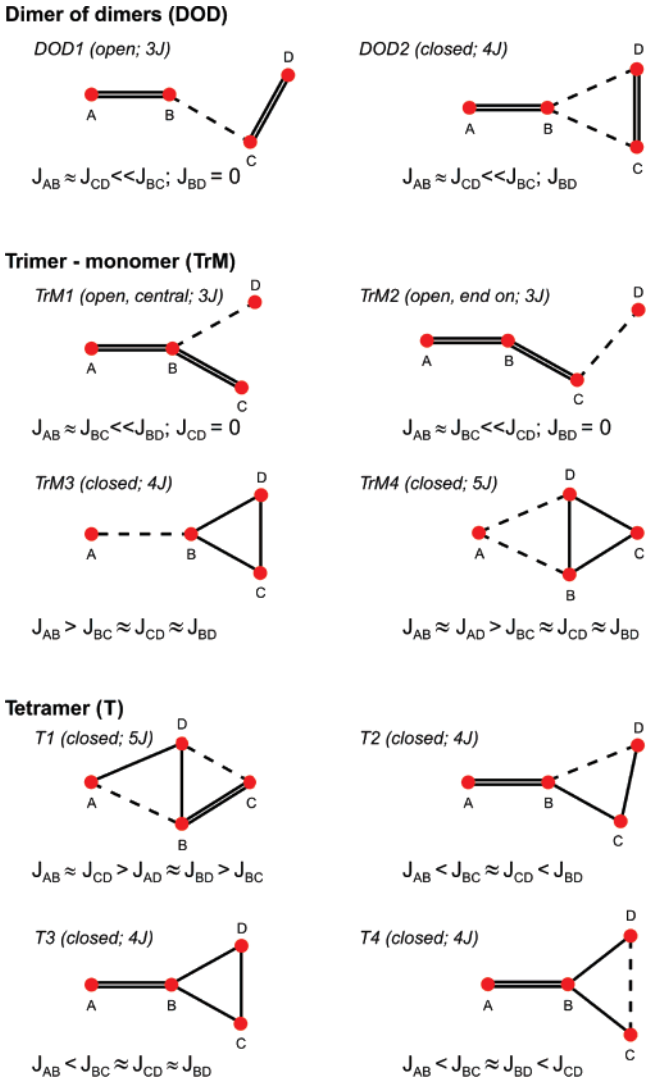

Figure 7. Selected coupling schemes for the Mn_4O_xCa cluster of photosystem II in the S_2 state that are consistent with currently proposed structural models that fit into the overall shape of the electron density of this cluster derived by X-ray crystallography.[20,24,25,27] The coupling schemes are grouped into (i) dimer of dimers (DOD), (ii) trimer−monomers (TrM), and (iii) tetramers (T). The red dots represent the four Mn ions. The Ca ion is not included, since coupling via Ca is assumed to be negligible. The coupling strength is indicated by the type of connecting lines. Solid double lines, strong antiferromagnetic coupling (-250 cm^{-1} to -100 cm^{-1}); solid lines, medium antiferromagnetic coupling (-100 cm^{-1} to -20 cm^{-1}); dashed lines, weak antiferro- or ferromagnetic coupling (-20 cm^{-1} to $+20$ cm^{-1}). If not otherwise mentioned $J_{AC} = J_{AD} = 0$. Several of the presented coupling schemes were previously proposed or have been derived as described in the text from proposed structural models: DOD1,[33,89,90] DOD2,[57,89,91] TrM1,[23] TrM2,[23,37] TrM3,[23,35,62,92,93] TrM4,[27,85,94−97] T1,[88] T2,[21,62,93] T4.[62,93] For more details see text and Supporting Information.

lines. In this representation the geometric model of Figure 1b,c corresponds to the electronic structure of the T2-type tetramer in Figure 7.

It is important to point out that our general Y-shaped coupling scheme (Figure 1c, right side) can describe all 3*J* and 4*J* schemes shown in Figure 7 (i.e., all schemes except for TrM4 and T1), if no specific restriction for the relative strengths of the J_{ik} values are implied (for details see the Experimental Section "Search protocol ..."). Therefore, the results reported below for the general search for possible oxidation states of the S_0 and S_2 states are not restricted to the geometric structure shown in Figure 1b but covers all Y-shaped coupling schemes (Figure 7). Below we discuss the results of our general search for possible Mn oxidation states:

S_0 = Mn_4(II,III,III,III). No solutions were found for Mn(II) being Mn_A (see Figure 1c or Figure 7 for the labeling of the four Mn ions). For Mn_B(II) a small number of solutions was found, with typical values of $J_{AB} = -100$ cm^{-1}, $J_{BC} = -40$ cm^{-1}, $J_{BD} = -100$ cm^{-1}, $J_{CD} = -100$ cm^{-1}. According to Constraint II this solution is unrealistic, because $J_{BD} = -100$ cm^{-1} lies far out of the precedented range for Mn(II)−Mn(III) couplings. Similarly, all solutions found for Mn_C(II) have strongly antiferromagnetic (< -100 cm^{-1}) J_{BC} and J_{CD} couplings, which are well out of the range of Mn(II)−Mn(III) interactions. For Mn_D(II) the situation is practically the same; i.e., solutions exist only with J_{BD}, $J_{CD} < -100$ cm^{-1}. In summary, no *viable* solutions were found for the S_0 state with Mn_4(II,III,III,III) composition, with Mn(II) being in any of the four possible positions.

S_0 = Mn_4(II,II,III,IV). Solutions were found for four oxidation state sets, namely Mn_{ABCD}(IV,III,II,II), Mn_{ABCD}(III,IV,II,II), Mn_{ABCD}(II,II,III,IV), Mn_{ABCD}(II,II,IV,III). In the Mn_{ABCD} notation the oxidation states in the brackets are given in the order Mn_A, Mn_B, Mn_C, and Mn_D. All results imply medium to strong (< -30 cm^{-1}) antiferromagnetic Mn(II)−Mn(II) interactions, which are not realistic according to Constraint II. Therefore, no *viable* solutions were found for the S_0 state with Mn_4(II,II,III,IV) composition.

S_0 = Mn_4(II,III,IV,IV). The only solution found has Mn_{ABCD}(IV,III,IV,II) with $J_{AB} = +155$ cm^{-1}, $J_{BC} = -258$ cm^{-1}, $J_{CD} = -155$ cm^{-1}, $J_{BD} = -155$ cm^{-1}. Since the strongly ferromagnetic $J_{AB} = +155$ cm^{-1} coupling is out of the precedented range for Mn(III)−Mn (IV) couplings, and also $J_{CD} = J_{BD} = -155$ cm^{-1} are too strong for Mn(II)−Mn(III) and Mn(II)−Mn(IV) couplings (Constraint II), the S_0 state can also not have a Mn_4(II,III,IV,IV) composition.

S_0 = Mn_4(III,III,III,IV). A large number of solutions were found which fit all constraints imposed at this stage. Solutions exist with Mn(IV) being in each possible position. This overall oxidation state composition is therefore selected for a detailed search for the electronic structure of the S_0 state (see next section).

S_1 = Mn_4(III,III,IV,IV). Since our general search for the Mn oxidations states of the S_0 state excludes that the S_0 state contains a Mn(II) ion, and the $S_0 \rightarrow S_1$ transition is known to involve Mn oxidation,[32] the *low* valent option for the S_1 state (S_1 = Mn_4(III,III,III,III)) can be excluded and only the *high* valent option remains.

S_2 = Mn_4(III,IV,IV,IV). Since on the basis of EXAFS experiments also the $S_1 \rightarrow S_2$ transition is known to involve a Mn-centered oxidation of the OEC,[32,33] the only possible composition for the S_2 state is Mn_4(III,IV,IV,IV). Indeed, many solutions were found with this composition for S_2 that reproduced the experimental $A_{i,iso}$ values within 10%. A more detailed search for the electronic structure of the S_2 state is presented below.

Assignment of the Oxidation States to Individual Mn Ions. This task is best performed for specific structural models of the Mn_4O_xCa cluster, since open searches yield thousands of solutions for each position of the unique Mn(III) in S_2 and the unique Mn(IV) in the S_0 state even after filtering according to

Constraints I and II. Therefore, we apply a "T2(S_2)-structure filtering" (T2(S_2)-SF) that is based on the new EXAFS structure of the Mn_4O_xCa cluster (Figure 1b and c, and T2 in Figure 7).[21] This filtering involves narrowing the allowed ranges for the exchange coupling constants such that a specific order of their relative strengths is reached. The principles for this were already outlined in the previous section, where for the Mn_4O_5 core of the Mn_4O_xCa cluster[21] the relation $|J_{AB}| > |J_{BC}| \approx |J_{CD}| > |J_{BD}|$ was obtained for the involved antiferromagnetic exchange couplings (see T2 in Figure 7). Below we discuss the T2(S_2)-SF method in more detail.

In the S_1 and S_2 states the Mn_4O_5 unit comprises two 2.7 Å Mn−Mn distances (Mn_A−Mn_B and Mn_B−Mn_C), one 2.8 Å Mn_C−Mn_D distance, and one 3.3 Å Mn_B−Mn_C distance.[21,93] The Mn_A−Mn_B distance is a true bis-μ-oxo bridged moiety and should therefore have a strong antiferromagnetic coupling on the order of $-250\ cm^{-1} \le J_{AB} \le -100\ cm^{-1}$. J_{BC} and J_{CD} are expected to be weaker (medium strength; $-100\ cm^{-1}$ to $-20\ cm^{-1}$), because one of the μ-oxo bridges is of μ_3-type and geometrical constraints may further reduce the coupling strength. Since the Mn_C−Mn_D distance is slightly longer than Mn_B−Mn_C (2.8 Å vs 2.7 Å), it may also be expected that $|J_{BC}| \ge |J_{CD}|$. However, this latter point was not included in the structure filter. Finally, a weak ferro- or antiferromagnetic coupling is expected for the 3.3 Å Mn_B−Mn_D distance, because the two Mn centers are connected only via a μ_3-oxo bridge. We employ $-20 \le J_{BD} \le +20\ cm^{-1}$ for this weak coupling. EPR/ENDOR based arguments for excluding many of the other coupling schemes presented in Figure 7 are given in the Supporting Information.

S_2 = Mn_4(III,IV,IV,IV). Without the T2(S_2)-SF the number of solutions found for the Mn(III) ion being in each position is several thousand. The vast majority of these solutions are characterized by a strong J_{AB} coupling and three approximately similar medium strength couplings ($-110\ cm^{-1}$ to $-40\ cm^{-1}$) for J_{BC}, J_{CD}, and J_{BD} (model T3 in Figure 7). These solutions are qualitatively similar to those suggested by Charlot et al.[58] and are therefore not shown. However, these solutions are not easily reconcilable with the recent structural information from single-crystal EXAFS,[21] which clearly shows the presence of one 3.3 Å distance between Mn_B and Mn_D. As outlined above, this mono μ_3-bridged Mn pair is expected to have a weak coupling. This consideration is the strongest constraint imposed by the T2(S_2)-SF.

After filtering of this large set of solutions with the T2(S_2)-SF, only about 25 solutions remain at the step widths of our search grid. These solutions split about equally to Mn(III) being either in position A, "S_2(A)", or C, "S_2(C)" (Figure 8a and b). In contrast, no solutions are found for Mn(III) being in the other two positions (B and D).

The presentation of the solutions for the 4J spin-coupling schemes is similar to that introduced by Charlot and co-workers.[58] Each solution (the set of the exchange coupling constants J_{AB}, J_{BC}, J_{CD}, and J_{BD}) is represented by one symbol in the upper plot (J_{CD} vs J_{AB}) and by one in the lower plot (J_{BC} vs J_{AB}). The J_{BD} value is coded by the shape and the color of the symbols. For each possible value J_{AB} there are therefore two points with the same symbol that is coding the value of J_{BD} (the weakly coupled 3.3 Å distance): one in the lower part, giving the corresponding value of J_{BC}, and one in the upper part, giving the value of J_{CD} that belongs to this solution.

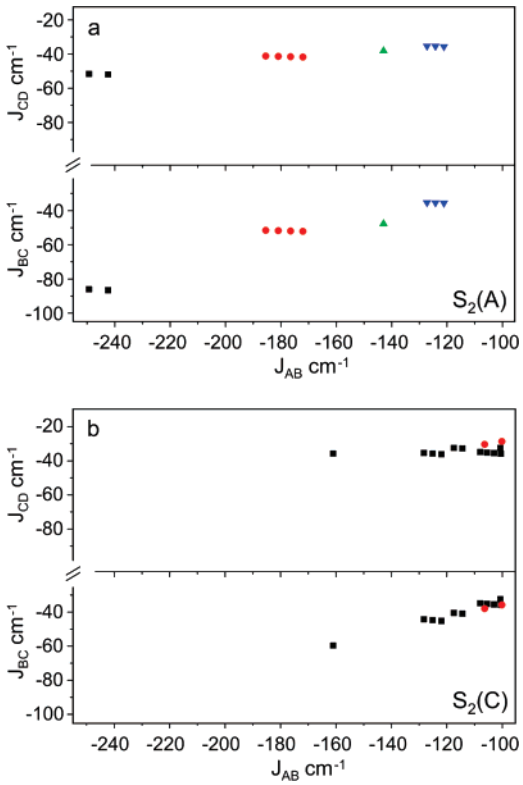

Figure 8. T2(S_2)-structure filtered (T2(S_2)-SF) solutions for J_{ik} in the S_2(A) state (panel a) and the S_2(C) state (panel b). The overall oxidation state for these two S_2 states is Mn_4(III,IV,IV,IV), with Mn_A = Mn(III) and Mn_C = Mn(III), respectively (see also Figure 9). The exchange coupling constants used are defined in Figure 1c. To each value of J_{AB} belong two corresponding points of the same symbol and color: one in the upper and one in the lower part of each panel. They are marking the values for J_{BC} (lower parts of panels a, b) and that of J_{CD} (upper parts of panels a, b). The value of the fourth involved exchange coupling constant J_{BD} is coded by the color and shape of the symbols: black squares, $J_{BD} = -10$ to $-20\ cm^{-1}$; red circles, $J_{BD} = -2$ to $-10\ cm^{-1}$; green triangles, $J_{BD} = 0\ cm^{-1}$; blue inverted triangles, $J_{BD} = +2$ to $+10\ cm^{-1}$.

As imposed by the T2(S_2)-SF J_{AB} is the largest coupling in the solutions presented in Figure 8a and b, because it describes the coupling via a true bis-μ-oxo bridged Mn_2 pair. Interestingly, for all solutions J_{BC} is about one-third of J_{AB}, and $|J_{BC}|$ is of similar value as $|J_{CD}|$. This can be easily seen by the fact that all points in Figure 8a and b lie along a diagonal. Similarly, the value of J_{BD} (coded by the symbols) decreases or increases together with the other J_{ik} couplings. This shows that certain ratios between the four exchange coupling constants J_{ik} are important for valid solutions for the S_2 state. It is important to point out that these relative values are only partially the consequence of the T2(S_2)-SF, because according to the above given accepted ranges also solutions with almost similar values for J_{AB}, J_{BC}, and J_{CD} would have been possible.

J_{BD} is usually weakly antiferromagnetic (-5 to $-20\ cm^{-1}$). However, also a few results exist with $+10 > J_{BD} > 0$ (blue inverted triangles) and one with $J_{BD} = 0$ (green triangle). Although the solution with $J_{BD} \approx 0$ appears at first glance to be similar to the trimer−monomer (or "dangler") solution suggested by Britt and co-workers,[37] the two models are indeed magnetically different. The $J_{BD} \approx 0$ solution is best described as an open tetramer (T2(S_2) in Figure 7, but with $J_{BD} = 0$), as

Table 3. Ranges for the Strength of the Exchange Coupling Constants of the Individual Mn Pairs in the Mn_4O_xCa Cluster Derived from the Detailed Search, i.e., after Application of the T2(S_2) and T2(S_0) Structure Filters

	Mn oxidation state				exchange coupling constants, cm^{-1}			
	A	B	C	D	J_{AB}	J_{BC}	J_{CD}	J_{BD}
S_2(A)	III	IV	IV	IV	-180 ± 60	-60 ± 25	-40 ± 10	-5 ± 15
S_2(C)	IV	IV	III	IV	-130 ± 30	-45 ± 15	-32 ± 5	-10 ± 8
S_0(A)	IV	III	III	III	-25 ± 10	-50 ± 25	-60 ± 40	-10 ± 10
S_0(B)	III	IV	III	III	-80 ± 60	-40 ± 15	-40 ± 15	-10 ± 10
S_0(C)	III	III	IV	III	-35 ± 15	-40 ± 20	-69 ± 10	-5 ± 15
S_0(D)	III	III	III	IV	-25 ± 10[a]	-50 ± 30	-40 ± 15	-5 ± 15

[a] A few points with $J_{AB} = -65$ cm^{-1} to -105 cm^{-1} and $J_{BD} < -10$ cm^{-1} were ignored for calculating the range for allowed J_{AB} values; see Figure S7 in the Supporting Information.

it has one strong and two medium strength couplings, while the "dangler" has two connected strong and a third weak coupling (Figure 7, models TrM1 and TrM2).

The ranges of possible couplings are summarized in Table 3, and selected examples for coupling schemes of the S_2 state with Mn(III) in the two possible positions are presented in Figure 9.

In the absence of methanol the S_2 state displays, at the expense of the S_2 MLS, the $g = 4.1$ ($S = {}^5/_2$) EPR signal in some of the PSII centers.[43,44,98] It was previously suggested that this can be explained by a Mn(III) $\leftrightarrow$ Mn(IV) valence flip between two Mn centers within the Mn_4O_xCa cluster.[58,64] While we are able to find solutions consistent with this proposal, we refrain from presenting them because (i) the lack of suitable restrains and (ii) the finding that preliminary ^{55}Mn-ENDOR experiments on S_2 state samples lacking methanol yield ^{55}Mn-ENDOR spectra that are clearly distinct from those presented above (see Figure S5 in the Supporting Information and ref 37). Therefore, analysis of such mixed-state samples, and of the $g = 4.1$ state, is beyond the scope of the present paper.

S_0 = Mn_4(III,III,III,IV). As pointed out before a huge number of possible solutions was found for each position of Mn(IV) in the absence of structure filtering. In contrast to the S_2 state, the large majority of these comprise a weak J_{AB}, with an absolute value that is similar or even smaller than $|J_{BC}|$ and $|J_{CD}|$. This significant change in coupling strength of J_{AB} is therefore a general result, which likely reflects (i) the significant difference between $A_{1,iso}$ between S_2 and S_0 (298 MHz vs 347 MHz; Table 1), (ii) the smaller intrinsic HFI constants of Mn(III) compared to Mn(IV) and the relative abundance of these

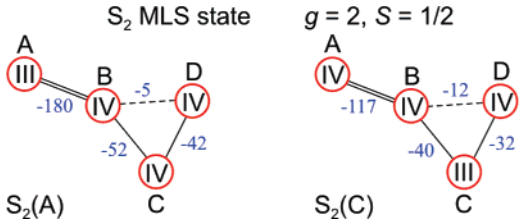

Figure 9. Selected spin-coupling schemes for the S_2 multiline state. The Mn ions are symbolized by red circles, and their oxidation states are given in roman numbers. The values for the exchange coupling constants are given in cm^{-1} in blue arabic numbers, and the relative strength of the couplings is shown as double, single, and broken lines as explained in the caption of Figure 7.

ions in the two S_n states, and (iii) the consequently greater spin projection values (spin densities) in the S_0 state. The consistently smaller coupling between Mn_A and Mn_B indicates a significant weakening of the Mn_A-Mn_B bridge(s) in the S_0 state as compared to the S_2 state. For the S_0 structure filter, T2(S_0)-SF, we therefore extended the range for J_{AB} to -250 $cm^{-1} \le J_{AB} \le +10$ cm^{-1}, while the other limits remained as specified for the S_2 state.

After applying the T2(S_0)-SF still a large number of schemes remain for Mn(IV) being in all possible positions. In Figure 10a and 10b, we display solutions for Mn(IV) being in positions B (S_0(B)) and C (S_0(C)). The results for S_0(A) and S_0(D) are quite similar to those for S_0(B) and S_0(C) and are therefore given in the Supporting Information (Figure S6 and S7). The corresponding ranges of couplings are listed in Table 3, and selected solutions are displayed for all cases in Figure 11.

It can be seen in Figure 10a that in apparent contradiction to the above general statement solutions are also found where $|J_{AB}|$ is clearly larger than $|J_{BC}|$ and $|J_{CD}|$. This is the case for S_0(B) when J_{BD} falls into the range between -10 and -20 cm^{-1}. However, also here $|J_{AB}|$ is for most cases only about one-half or less of the values found in the S_2 state with similar J_{BD} (compare black squares in Figures 10a and Figure 8a,b; we consider it unlikely that J_{BD} is more negative in S_0 than in the S_2 state). In all other cases the solutions for J_{AB} fall into the range -70 $cm^{-1} \le J_{AB} \le -10$ cm^{-1} (Figures 8a,b, S6, and S7). Therefore, the above comparison of the ^{55}Mn-ENDOR data of the S_2 state and the S_0 state strongly indicates that one μ-hydroxo bridge and one μ-oxo bridge are present between Mn_A and Mn_B in the S_0 state, while a bis-μ-oxo bridge motive exists in the S_2 state between these two Mn ions (Figure 12). Furthermore it shows that the structural model derived from polarized EXAFS on PSII single crystals[21] is fully consistent with current EPR and ^{55}Mn-ENDOR data of the S_0 and S_2 states.

Discussion

Determination of the Overall Manganese Oxidation States of the OEC. In earlier publications numerous hypotheses about the geometry and the oxidation states of Mn ions in the S_0 and S_2 states of the OEC were put forward. Since no pulse EPR and ENDOR data on the S_0 state were available at that time, the hypotheses concerning this state were based mainly on the analysis of the total width of the X-band CW EPR multiline spectrum of the S_0 state. In ref 47 a dinuclear Mn(II)Mn(III) model was suggested for the S_0 state. This model seems largely improbable in view of the present ^{55}Mn-ENDOR data, which show that all four Mn ions are magnetically coupled in the S_0

(89) Yachandra, V. K.; DeRose, V. J.; Latimer, M. J.; Mukerji, I.; Sauer, K.; Klein, M. P. *Science* **1993**, *260*, 675−679.
(90) Dau, H.; Iuzzolino, L.; Dittmer, J. *Biochim. Biophys. Acta* **2001**, *1503*, 24−39.
(91) Kusunoki, M., Mechanism of the photosynthetic water oxidation reaction catalyzed by a noble Mn_4CaCl-bicarbonate cluster. In *Photosynthesis: Fundamental Aspects to Global Perspectives*; van der Est, A.; Bruce, D., Eds.; Alliance Communications Group: Lawrence, KS, 2005; Vol. 1, pp 410−412.
(92) George, G. N.; Prince, R. C.; Cramer, S. P. *Science* **1989**, *243*, 789−791.
(93) Yano, J.; Pushkar, Y.; Glatzel, P.; Lewis, A.; Sauer, K.; Messinger, J.; Bergmann, U.; Yachandra, V. K. *J. Am. Chem. Soc.* **2005**, *127*, 14974−14975.
(94) McEvoy, J. P.; Brudvig, G. W. *Phys. Chem. Chem. Phys.* **2004**, *6*, 4754−4763.
(95) McEvoy, J. P.; Gascon, J. A.; Batista, V. S.; Brudvig, G. W. *Photochem. Photobiol. Sci.* **2005**, *4*, 940−949.
(96) Sproviero, E. M.; Gascon, J. A.; McEvoy, J. P.; Brudvig, G. W.; Batista, V. S. *J. Chem. Theory Comput.* **2006**, *2*, 1119−1134.
(97) Siegbahn, P. E. M.; Lundberg, M. *J. Inorg. Biochem.* **2006**, *100*, 1035−1040.
(98) Boussac, A.; Rutherford, A. W. *Biochim. Biophys. Acta* **2000**, *1457*, 145−156.

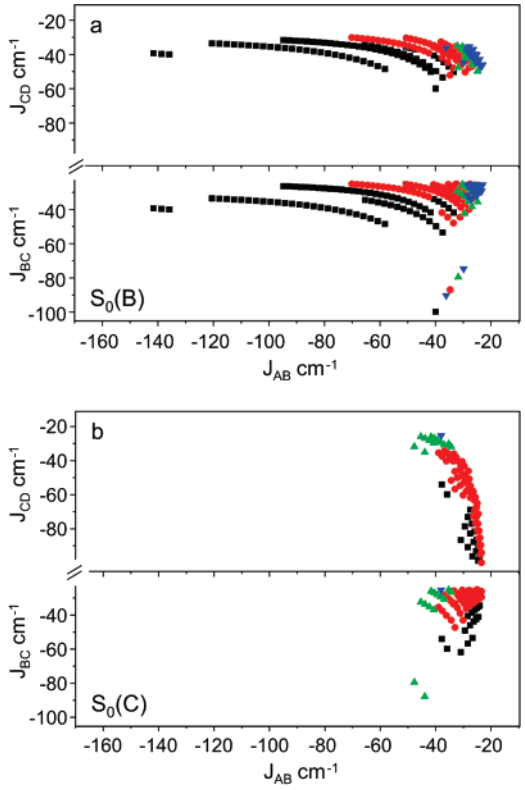

Figure 10. T2(S$_0$)-SF solutions for J_{ik} in the S$_0$(B) state (panel a) and the S$_2$(C) state (panel b). The overall oxidation state for these two S$_0$ states is Mn$_4$(III,III,III,IV), with Mn$_B$ = Mn(IV) and Mn$_C$ = Mn(IV), respectively (see also Figure 11). The exchange coupling constants used are defined in Figure 1c. To each value of J_{AB} belong two corresponding points of the same symbol and color: one in the upper and one in the lower part of each panel. They are marking the values for J_{BC} (lower parts of panels a, b) and that of J_{CD} (upper parts of panels a, b). The value of the fourth involved exchange coupling constant J_{BD} is coded by the color and shape of the symbols: black squares, $J_{BD} = -10$ to -20 cm^{-1}; red circles, $J_{BD} = -2$ to -10 cm^{-1}; green triangles, $J_{BD} = 0$ cm^{-1}; blue inverted triangles, $J_{BD} = +2$ to $+10$ cm^{-1}. Similar solutions have been obtained for S$_0$(A) and S$_0$(D), which are presented in the Supporting Information (Figures S6 and S7).

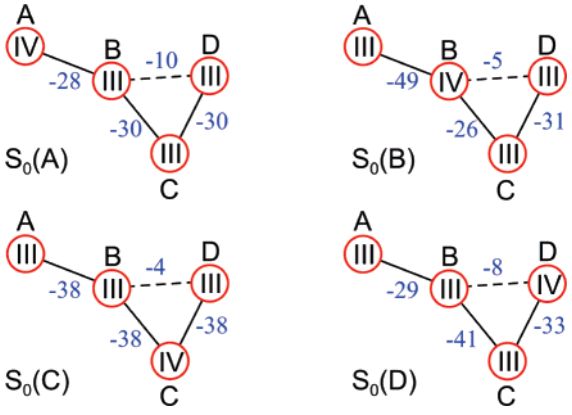

Figure 11. Selected spin-coupling schemes for the S$_0$ state, specifying individual Mn oxidation states in roman numbers and the exchange couplings constants, J_{ik}, in cm^{-1} (blue arabic numbers). Mn ions are symbolized by red circles, and the connecting lines represent the relative coupling strength (see Figure 7).

state.[40] Dismukes et al.[57] suggested a tetranuclear composition with a Mn$_4$(II,III,III,III) assignment for the S$_0$ state, based on EPR spectra simulations indicating a Mn$_4$(III,III,III,IV) oxidation state for the S$_2$ state. Since we do not find a valid solution for

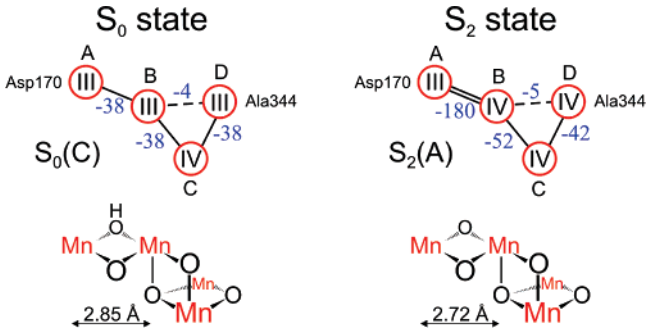

Figure 12. Top: Preferred spin-coupling schemes for the S$_0$ and S$_2$ states of the Mn$_4$O$_x$Ca cluster in photosystem II, which specify the individual Mn oxidation states (roman numbers) and the exchange couplings, J_{ik}, (blue arabic numbers; in cm^{-1}) between the Mn ions (red circles). The relative coupling strength is represented by the type of connecting lines between Mn ions (see Figure 7 for details). These preferred models allow a molecular understanding of previously reported[21,62] structural changes between the S$_0$ and S$_2$ states (lower row). For details see text and Figure 13.

the S$_0$ state that contains one or more Mn(II) ions, also this suggestion is strongly disfavored by the present results.

The tetranuclear composition of the S$_0$ state with two possible sets of Mn oxidation states, Mn$_4$(II,III,IV,IV) and Mn$_4$(III,III,III,IV), was discussed previously by Messinger et al.[32,45,46] Only the latter option is consistent with the present experimental data and the results of our extensive calculations. This is in agreement with our previous qualitative interpretation of the ^{55}Mn-ENDOR data[40] and the previous assignment of Mn$_4$(III,III,III,IV) to S$_0$ by Kusunoki.[88] We found, however, that simulations with the fit parameters reported by Kusunoki[88] lead to significant deviations from our measured Q-band EPR and ^{55}Mn-ENDOR data of the S$_0$ state (Figures S3 and S4).

This result not only settles the question about the overall oxidation states of the S$_0$ MLS state but simultaneously also answers the question about the redox level of the S$_1$ and S$_2$ states. On the basis of our results only the *high valent* option[32,37,59,89] remains viable and therefore the overall oxidation states of S$_0$, S$_1$, and S$_2$ are as follows:

S$_0$ = Mn$_4$(III,III,III,IV)
S$_1$ = Mn$_4$(III,III,IV,IV)
S$_2$ = Mn$_4$(III,IV,IV,IV).

We presently cannot exclude that methanol binding to the S$_0$ state leads to a redistribution of valences within the Mn$_4$O$_x$Ca cluster. Thus it remains a possibility that the overall oxidation state of S$_0$ in a methanol-free PSII sample is Mn$_4$(II,III,IV,IV). Since the XANES spectra of methanol-containing and methanol-free spinach PSII membrane fragments are very similar, we regard this option as not very likely. We like to point out that the conclusion about the overall oxidation states of the Mn$_4$O$_x$Ca cluster is independent of this question.

Assignment of the Oxidation States to Specific Mn Ions within the OEC. In our study several possible coupling schemes were derived for the S$_0$ and S$_2$ states that are consistent with the latest structural information about the Mn$_4$O$_x$Ca cluster.[21] Selected examples are displayed in Figures 9 (S$_2$ state) and 11 (S$_0$ state). The main difference between these options is the position of the unique Mn oxidation state.

It is not straight forward to identify the most likely redox state assignment. However, most solutions for the S$_0$ state have -50 cm$^{-1} \leq J_{AB}$ (see Figures 10, S6, and S7). On the basis of the following chain of arguments this finding is indicative of a

$Mn_A^{III}(-O-)(-OH-)Mn_B^{III}$ motif in the S_0 state: (i) It has been shown that protonation of one μ-oxo bridge in a $Mn^{IV}(-O-)_2Mn^{IV}$ complex reduces the coupling strength from $J = -184$ cm^{-1} to -96 cm^{-1}, i.e., by about one-half.[99] (ii) Since $Mn^{III}(-O-)_2Mn^{IV}$ complexes generally have couplings very similar to those of the corresponding $Mn^{IV}(-O-)_2Mn^{IV}$ complexes (see Constraint II) we assume that $Mn^{III}(-O-)(-OH-)Mn^{IV}$ also has an exchange coupling on the order of -90 cm^{-1} to -100 cm^{-1}, i.e., significantly stronger than that found in our simulations for the S_0 state. (iii) If one accepts the latter argument, then only S_0(C) and S_0(D) (Figure 11) remain viable, because they have a $Mn_A^{III}(-O-)(-OH-)Mn_B^{III}$ moiety. S_0(C) can convert into S_2(A) by oxidation of Mn_B (S_1 state) and then Mn_D (vide infra). It is unlikely to convert into S_2(C), because this would involve a redox-state switch between two Mn ions within the cluster. S_0(D) can convert into S_2(A) by first oxidizing Mn_B (vide infra) and then Mn_C and into S_2(C) by oxidation of Mn_A and Mn_B.

A further selection among the remaining two models for S_0 (S_0(C) and S_0(D)) and the two for S_2 (S_2(A) and S_2(C)) can be attempted on the basis of recent FTIR studies by Debus, Hillier and co-workers (Constraint IV).

(a) From the absence of vibrational changes in the carboxy group of D1Asp170 these authors concluded that this amino acid does not ligate a Mn ion that is oxidized during the S_n state cycle.[100] Ligation of D1Asp170 to Mn is supported by ESEEM studies[101,102] that demonstrate the involvement of this side chain during the photoassembly of the Mn_4O_xCa cluster.[103] Similarly, the recent single-crystal EXAFS data[21] show in combination with the PSII crystal structure of Loll et al.[20] that D1Asp170 is located in the vicinity of Mn_A (see also Figure 1b). These data can therefore be taken as an indication that Mn_A does not change redox states during S_n state turnovers. Since in both remaining S_0 options (S_0(C) and S_0(D)) Mn_A is in oxidation state III, this constraint implies that Mn_A stays Mn_A(III) throughout the Kok cycle. This argument therefore favors S_2(A) over S_2(C), since the latter contains Mn(IV) in position A.

(b) In a second study the same group showed that the Mn, which is ligated by the D1 C-terminus (D1Ala344), is oxidized during the $S_1 \rightarrow S_2$ transition.[104] On the basis of the most recent crystal structure[20] and the single-crystal EXAFS measurements[21] D1Ala344 (C-terminus) ligates Mn_D. In line with this idea S_2(A) has Mn(IV) in position D. From the two remaining S_0 models (S_0(C) and S_0(D); Figure 11), only S_0(C) has a Mn(III) ion in position D. This makes S_0(C) the favorable option for the S_0 state.

Although we agree that it is currently unclear to what extent a redox change of one metal center within a coupled cluster like the OEC will affect carboxy vibrations of its ligands,[18,96,105] we still feel that present experimental evidence favors the electronic structures S_0(C) and S_2(A) over the other two options. This preferred solution is displayed in the top part of Figure 12.

Simulations of the experimental ^{55}Mn-ENDOR spectra (Figures 2 and 6) with the directly derived values of magnetic parameters for the S_0 and S_2 states reproduce well the shape of the experimental data. However, the spectra calculated with isotropic Mn-HFI parameters based on the spin coupling schemes of Figure 12 and catalase-derived intrinsic isotropic Mn-HFI values are shifted to higher radio frequencies. This indicates that the isotropic intrinsic Mn−HFI parameters $a_{i,\mathrm{iso}}$ of several Mn ions in the OEC are smaller by 5−10% than those determined for Mn catalase.[82] This is consistent with Constraint I.

Finally, the possible influence of ZFS on the $A_{i,\mathrm{iso}}$ values has to be evaluated to assess possible deviations from eq 8. For this, ZFS is considered only for Mn(III), since for Mn(IV) this effect is usually much weaker. Calculations of the principal values of ρ_i were done for the S_0 and S_2 states with Mn oxidation states and exchange couplings as shown in Figure 12 by employing eq 10 and including the ZFS term into eq 9. The value of the ZFS parameter was chosen to be $D = 2.5$ cm^{-1}, which is close to the upper limit of the precedented ZFS values for Mn(III) ions. For simplicity, initially only Mn_A(III) was assumed to display ZFS, and the ZFS was considered with axial symmetry and the distortion axis was taken parallel to the hyperfine distortion axes. Together with an assumed degree of intrinsic HFI anisotropy $a_{\mathrm{aniso}}/a_{\mathrm{iso}} = 0.4$ the deviation from eq 8 was about 5% for the S_0 state and 2% for the S_2 state. In the case of several Mn(III) ions with non-negligible ZFS, the individual effects can add up or cancel depending on their mutual orientations. On that basis the deviation is likely to be below 10% but may add up to about 15%. This analysis shows that for typical cases the expected effect of ZFS on the $A_{i,\mathrm{iso}}$ is small enough to allow us to use eq 8 as a reasonable approximation. Similar results were obtained if one of the other Mn(III) ions were assumed to display intrinsic HFI anisotropy.

Structural Changes of the Mn_4O_xCa Cluster. EXAFS measurements on the S_0 state showed that there is a shortening of one Mn−Mn distance from 2.85 Å in the S_0 state to about 2.72 Å in the S_1 state.[33,62] On the basis of comparisons to model studies[99] this was tentatively assigned to the deprotonation of a μ-OH bridge. We show in this study that for the vast majority of cases J_{AB} is significantly smaller in the S_0 state as compared to the S_2 state, while the other couplings hardly change. This allows for the first time the assignment of a structural change within the Mn_4O_xCa cluster to a specific Mn−Mn bridge, namely that between Mn_A and Mn_B. This first step toward a real molecular understanding of the mechanism of water oxidation is illustrated in the lower part of Figure 12, employing the structure for the Mn_4O_5 core of the Mn_4O_xCa cluster that was recently determined by polarized EXAFS on PSII single crystals.[21]

Molecular Interpretation of the $S_0 \rightarrow S_1$ and $S_1 \rightarrow S_2$ Transitions. The above analysis allows the formulation of a

(99) Baldwin, M. J.; Stemmler, T. L.; Riggs-Gelasco, P. J.; Kirk, M. L.; Penner-Hahn, J. E.; Pecoraro, V. L. *J. Am. Chem. Soc.* **1994**, *116*, 11349−11356.
(100) Debus, R. J.; Strickler, M. A.; Walker, L. M.; Hillier, W. *Biochemistry* **2005**, *44*, 1367−1374.
(101) Campbell, K. A.; Force, D. A.; Nixon, P. J.; Dole, F.; Diner, B. A.; Britt, R. D. *J. Am. Chem. Soc.* **2000**, *122*, 3754−3761.
(102) Debus, R. J.; Aznar, C.; Campbell, K. A.; Gregor, W.; Diner, B. A.; Britt, R. D. *Biochemistry* **2003**, *42*, 10600−10608.
(103) Dismukes, C.; Ananyev, G. M.; Watt, R. Photo-assembly of the catalytic manganese cluster. In *Photosystem II. The Light-Driven Water:Plastoquinone Oxidoredutase*; Wydrzynski, T., Satoh, K., Eds.; Advances in Photosynthesis and Respiration; Springer: Dordrecht, 2005; Vol. 22, pp 609−626.
(104) Chu, H. A.; Hillier, W.; Debus, R. J. *Biochemistry* **2004**, *43*, 3152−3166.
(105) Sproviero, E. M.; Gascon, J. A.; McEvoy, J. P.; Brudvig, G. W.; Batista, V. S. *J. Inorg. Biochem.* **2006**, *100*, 786−800.

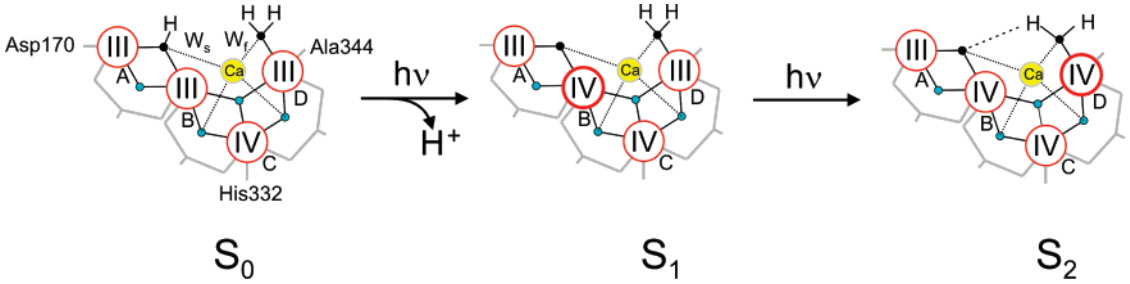

Figure 13. Molecular interpretation of the $S_0 \rightarrow S_1$ and $S_1 \rightarrow S_2$ transitions. The oxygen atoms of the slow (W_s) and fast (W_f) exchanging substrate water molecules are indicated as black dots. W_s is identified here with the μ-OH/μ-O bridge between Mn_A and Mn_B. Since currently available information on μ-O bridge exchange rates indicate that such bridges exchange with slower rates than those measured for W_s,[106−108] this suggestion implies that in PSII a special exchange mechanism may be operative, for example, via a terminal water ligand bound to Mn_A or Ca. Alternatively, W_s may bind to Mn_B as a terminal ligand (for this the suggested ligation sphere needs to be varied). Exchange of Ca against Sr modifies the substrate water exchange rates (especially of W_s),[109] and therefore Ca is suggested to participate in substrate water binding. The gray "clamps" stand for D1Glu333, CP43Glu354, and D1Asp342 (from left to right), which are assumed to be bidentate ligands of the Mn_4O_xCa cluster.

molecular mechanism for the first steps of the water oxidation cycle. For this we add to the structural model of the Mn_4O_xCa cluster[21] a reasonable ligation sphere. This is schematically shown in Figure 13 in light gray. The ligand arrangement is inspired by the approximate ligation sphere given in Figure S6 by Yano et al.[21] For clarity only those amino acids are specified that are discussed in the text. Other ligands are thought to be D1Glu333, CP43Glu354, and D1Asp342 (from left to right in the structures of Figure 13). Possible binding sites for the fast and the slowly exchanging substrate water molecules (W_f and W_s, respectively) are shown as black dots in Figure 13.

$S_0 \rightarrow S_1$ Transition: The central Mn_B(III) is oxidized to Mn_B(IV). This event triggers (i) the deprotonation of the μ_2-hydroxo bridge between Mn_A and Mn_B, (ii) the contraction of this distance from 2.85 Å to 2.72 Å,[33,62] and (iii) the slowing of the substrate water exchange rate of the slowly exchanging substrate water molecule, W_s, by a factor of 600.[110] The fast exchanging substrate water molecule, W_f, is assumed to be bound already in the S_0 state but exchanges so rapidly in the S_0 and S_1 states that it escapes detection with the current time resolution of 4−8 ms of the mass spectrometry experiments.[12,111]

$S_1 \rightarrow S_2$ Transition: In this transition, Mn_D, which is ligated to D1Ala344, is oxidized from Mn_D(III) to Mn_D(IV)[104] and W_f becomes detectable for the first time in the cycle.[112] W_f either is not deprotonated or transfers the proton within an H-bridge to a nearby residue. For simplicity and because the exchange of W_s is faster by a factor of 100 in the S_2 state compared to S_1, we suggest that a weak H-bridge is formed between one proton of W_f and the Mn_A−O−Mn_B μ-oxo bridge (W_s), which is geometrically quite close.

It is important to consider that at cryogenic temperatures the S_2 state can be trapped in at least two different electronic configurations (S_2 MLS state and $g = 4.1$ state; for a recent account see ref 113), from which we studied only the more prominent and stable S_2 multiline state. The functional relevance of other electronic/geometric configurations of this and possibly other S_n states needs to be elucidated in the future. Further studies on the S_3 and S_4 states are required for a detailed description of the remaining transitions leading to the formation of molecular oxygen from water.

Conclusions

In this paper the overall manganese oxidation states of the OEC in the S_0 and S_2 states were determined for methanol containing (3%) spinach PSII membrane fragments, and in addition, specific oxidation state assignments were presented for the individual Mn ions in the S_0, S_1, and S_2 states. The large number of initial solutions for the S_0 and S_2 states show that ^{55}Mn-ENDOR data by themselves are not a very sharp tool for selecting the correct geometry and electronic structure of the Mn_4O_xCa cluster. However, in combination with reliable structural information about the Mn_4O_xCa cluster[21] ^{55}Mn-ENDOR spectroscopy becomes a powerful tool for deriving possible electronic configurations of paramagnetic states, especially if two different electronic states (S_0 and S_2) are analyzed in parallel. Application of reasonable structural filters together with data from the literature lead to a molecular description of the first two S_n state transitions that appears to be consistent with most experimental results. One has to keep in mind, however, that this involves an extrapolation of the low temperature (10 K) experimental data to room temperature (270−300 K), where photosynthetic water splitting occurs. So far it is unknown to which extent the electronic and/or geometric structures vary at these different temperatures.[114] However, XANES and EXAFS experiments at room temperature did not reveal any significant changes as compared to those at 10 K.[115] It can therefore be assumed that the insight gained in this study about the electronic and geometric structures of the S_0, S_1, and S_2 states is of functional relevance. The above analysis shows that the Mn_4O_xCa cluster actively takes part in the unique water splitting chemistry via structural changes, of which one can now be located within the cluster. We hope that these results will further inspire the much needed development of artificial catalysts for solar water splitting.

(106) Messinger, J.; Badger, M.; Wydrzynski, T. *Proc. Natl. Acad. Sci. U.S.A.* **1995**, *92*, 3209−3213.
(107) Hillier, W.; Wydrzynski, T. *Biochim. Biophys. Acta* **2001**, *1503*, 197−209.
(108) Tagore, R.; Chen, H. Y.; Crabtree, R. H.; Brudvig, G. W. *J. Am. Chem. Soc.* **2006**, *128*, 9457−9465.
(109) Hendry, G.; Wydrzynski, T. *Biochemistry* **2003**, *42*, 6209−6217.
(110) Hillier, W.; Wydrzynski, T. *Biochemistry* **2000**, *39*, 4399−4405.
(111) Konermann, L.; Messinger, J.; Hillier, W., Mass spectrometry based methods for studying kinetics and dynamics in biological systems. In *Biophysical Techniques in Photosynthesis (Volume II)*; Aartsma, T. J., Matysik, J., Eds.; Advances in Photosynthesis and Respiration; Springer: Dordrecht, 2008; Vol. 26, pp 167−190.
(112) Hendry, G.; Wydrzynski, T. *Biochemistry* **2002**, *41*, 13328−13334.
(113) Sioros, G.; Koulougliotis, D.; Karapanagos, G.; Petrouleas, V. *Biochemistry* **2007**, *46*, 210−217.
(114) Renger, G. *Photosynthetica* **1987**, *21*, 203−224.
(115) Haumann, M.; Grabolle, M.; Neisius, T.; Dau, H. *FEBS Lett.* **2002**, *512*, 116−120.

Acknowledgment. This work is dedicated to Prof. Karl Wieghardt (MPI für Bioanorganische Chemie, Mülheim an der Ruhr) on the occasion of his 65th birthday. The authors thank Eckhard Bill, Marco Flores, Gernot Renger, Karl Wieghardt, Vittal Yachandra, and Junko Yano for discussions. Financial support by the Alexander von Humboldt Foundation (L.K.), the President of the Russian Federation Grant for Young Scientists (MK-7440.2006.3 to L.K.), the Russian Science Support Foundation (L.K.), the DFG (J.M.; Me 1629/2-3 and 2-4), the EU (Solar-H), the BMFT ($BioH_2$), and the Max-Planck Society is gratefully acknowledged.

Supporting Information Available: Flow diagrams (FD1 to FD4) illustrating the analysis procedure; Q-band EPR and ^{55}Mn-ENDOR simulations of the S_0 and S_2 states based on parameters determined previously by other authors (figures and text); discussion of previously proposed spin coupling schemes displayed in Figure 7; figure of the ^{55}Mn-ENDOR spectrum of the S_2 state in the absence of methanol; T2(S0)-SF filtered coupling schemes for the S_0(A) and S_0(D) states. This information is available free of charge at http://pubs.acs.org.

JA071487F